

# The Open DAC 2025 Dataset for Sorbent Discovery in Direct Air Capture

Anuroop Sriram<sup>1,\*</sup>, Logan M. Brabson<sup>2,\*</sup>, Xiaohan Yu<sup>2,\*</sup>, Sihoon Choi<sup>2</sup>, Kareem Abdelmaqsoud<sup>5</sup>, Elias Moubarak<sup>4</sup>, Pim de Haan<sup>4</sup>, Sindy Löwe<sup>4</sup>, Johann Brehmer<sup>4</sup>, John R. Kitchin<sup>5</sup>, Max Welling<sup>4</sup>, C. Lawrence Zitnick<sup>1</sup>, Zachary Ulissi<sup>1</sup>, Andrew J. Medford<sup>2</sup>, David S. Sholl<sup>3</sup>

<sup>1</sup>FAIR at Meta, <sup>2</sup>School of Chemical and Biomolecular Engineering, Georgia Institute of Technology, <sup>3</sup>University of Tennessee-Oak Ridge Innovation Institute, Oak Ridge National Laboratory, <sup>4</sup>CuspAI, <sup>5</sup>Department of Chemical Engineering, Carnegie Mellon University

\*Equal contribution

Identifying useful sorbent materials for direct air capture (DAC) from humid air remains a challenge. We present the Open DAC 2025 (ODAC25) dataset, a significant expansion and improvement upon ODAC23 (Sriram et al., ACS Central Science, 10 (2024) 923), comprising nearly 70 million DFT single-point calculations for CO<sub>2</sub>, H<sub>2</sub>O, N<sub>2</sub>, and O<sub>2</sub> adsorption in 15,000 MOFs. ODAC25 introduces chemical and configurational diversity through functionalized MOFs, high-energy GCMC-derived placements, and synthetically generated frameworks. ODAC25 also significantly improves upon the accuracy of DFT calculations and the treatment of flexible MOFs in ODAC23. Along with the dataset, we release new state-of-the-art machine-learned interatomic potentials trained on ODAC25 and evaluate them on adsorption energy and Henry’s law coefficient predictions.

**Date:** August 6, 2025

**Correspondence:** A.S. [anuroops@meta.com](mailto:anuroops@meta.com), A.J.M ([ajm@gatech.edu](mailto:ajm@gatech.edu)), D.S.S ([shollds@ornl.gov](mailto:shollds@ornl.gov))

**Code:** <https://github.com/facebookresearch/fairchem>



## 1 Introduction

Direct air capture (DAC) represents a promising carbon capture technology for addressing global climate change through negative emissions [1]. Unlike traditional point-source capture, DAC facilities can operate at ambient conditions with fewer geographical constraints [2]. However, most existing DAC sorbents require energy-intensive regeneration that increases costs and reduces environmental benefits [3]. Metal-organic frameworks (MOFs) [4] offer a promising alternative as highly tunable, modular porous materials with potential for low-temperature sorbent regeneration [5, 6]. Given the vast chemical space and synthesis challenges of MOFs [7–9], high-throughput computational screening (HTCS) has become essential for developing better sorbents [10, 11].

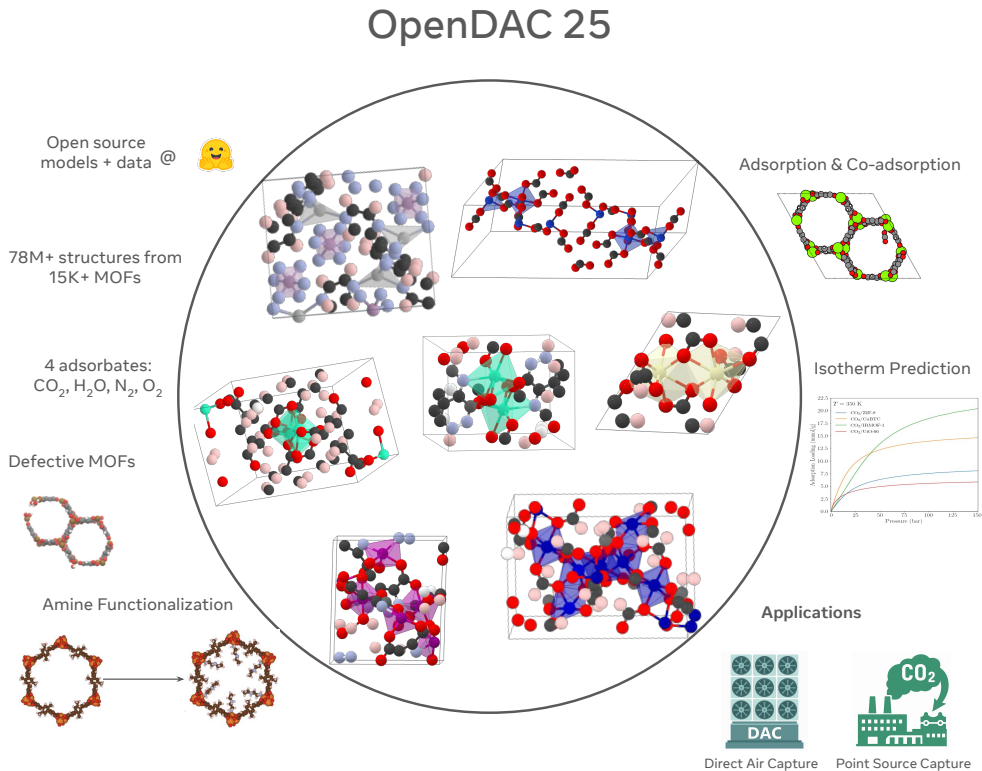


**Figure 1** Overview of the ODAC25 dataset generation, application areas, and sampling strategies.

The Open DAC 2023 (ODAC23) dataset [12] introduced over 38 million DFT calculations for  $\text{CO}_2$  and  $\text{H}_2\text{O}$  adsorption across 8,400 MOFs, identifying interesting candidates for DAC and the influence of key chemical motifs such as open-metal sites, parallel aromatic rings, metal-oxygen-metal bridges, and uncoordinated nitrogen atoms. Prior HTCS studies relying on classical force fields [13] such as UFF(4MOF) [14–16] and rigid framework assumptions often failed to identify viable materials [17–20]. By incorporating framework flexibility and DFT-level accuracy, ODAC23 identified MOF sites with potential  $\text{CO}_2$  selectivity that classical approaches missed. While DFT calculations are computationally expensive for large-scale screening, machine learning force fields (MLFFs) trained on this DFT data demonstrated the promise of approaching this level of accuracy while dramatically accelerating high-throughput screening.

Despite its advances, ODAC23 had limitations. First, it was limited to two adsorbates,  $\text{CO}_2$  and  $\text{H}_2\text{O}$ , while realistic air separations require modeling  $\text{N}_2$  and  $\text{O}_2$  as well. Second, ODAC23 did not explore functionalization of MOF linkers or open metal sites (OMSs) [21, 22], approaches that offer significant potential to enhance  $\text{CO}_2$  selectivity while reducing regeneration energy [23, 24]. Third, ODAC23 reported only adsorption energies relative to relaxed empty MOF structures, potentially introducing artifacts when guest molecules stabilized MOFs into lower-energy configurations than the empty framework reference state.

These limitations, combined with ongoing challenges around MOF structural integrity in computational studies [25, 26], motivated the development of a more comprehensive and methodologically rigorous dataset.

Recent advances in machine learning force fields (MLFFs) have enabled accurate prediction of molecular and materials properties at significantly reduced computational cost compared to ab initio methods. While MLFFs have shown promise in modeling adsorbate–framework interactions in MOFs, large-scale screening for DAC presents multiple challenges, including: low concentrations of CO<sub>2</sub>, presence of competing gases (N<sub>2</sub>, O<sub>2</sub>, and H<sub>2</sub>O), and spatially and chemically heterogeneous binding environments. This requires the MLFFs to generalize across a broad range of framework topologies, adsorbates, and placement configurations.

To address these limitations, we introduce in this paper the Open Direct Air Capture 2025 (ODAC25) dataset (figure 1) comprising nearly 70 million DFT calculations across 15,000 MOFs with four adsorbates: CO<sub>2</sub>, N<sub>2</sub>, O<sub>2</sub>, and H<sub>2</sub>O. ODAC25 substantially expands ODAC23 in terms of scale, diversity, and computational accuracy. We systematically improved the accuracy of all calculations by performing various MOF validation checks, correcting for systematic errors introduced by incompletely converged k-point sampling, and re-relaxing each bare MOF structure to account for adsorbate-induced MOF deformation. ODAC25 improves upon the diversity of ODAC23 by including functionalized MOFs with both linker and open-metal site (OMS) functionalization, synthetically generated frameworks that extend structural and chemical diversity beyond what is available in experimental databases, as well as high-energy multi-component adsorption configurations derived from Grand Canonical Monte Carlo (GCMC) simulations. ODAC25 is thus designed not only to improve MLFF performance, but also to support realistic benchmarking and sorbent screening for DAC and other applications of MOFs.

We also release a suite of state-of-the-art MLFFs (EquiformerV2 [27], eSEN [28], and UMA [29]) trained on ODAC25 and benchmarked on prediction of energies and forces, as well as Henry’s law coefficients computed with MLFFs using Widom insertion.

## 2 Results: ODAC25 Dataset

ODAC25 introduces several improvements over ODAC23 that can be broadly categorized into two groups: improvements to DFT calculation accuracy (section 2.1) and improvements to the diversity of the dataset (section 2.2).

### 2.1 Accuracy and Data Quality

#### 2.1.1 Validation of MOF structures

The first improvement introduced by ODAC25 addresses the chemical validity of the dataset’s MOFs. White et al. [25] suggested that high rates of structural errors exist in some MOF databases, including ODAC23, by applying an algorithm based on semi-empirical calculations to check metal oxidation states. Jin et al. [30] released an algorithm to validate and correct MOF structural files called MOFChecker. To mitigate concerns related to MOF structural

accuracy, we performed several checks on all structures in ODAC25 using MOFChecker v0.9.6 [30]. Table S1 shows the checks performed and the percentage of ODAC25 structures that fail each. Jin et al. also screened ODAC23 MOFs for net charges according to stoichiometry and metal oxidation state predictions built into MOFChecker v2, and those results are available in their report [26].

We note that the validity of semi-empirical oxidation states and similar measures to assess the quality of MOFs is unclear. The MOF structures in ODAC23 and ODAC25 are fully relaxed with DFT calculations in charge-neutral periodic cells. Atomic point charges can be assigned from the electron distribution in these DFT calculations using DDEC charges [31] and related methods [32, 33]. For these reasons, we retained MOFs flagged as problematic by MOFChecker, and users may choose either the “*filtered*” or “*full*” dataset depending on their application. All discussion in this work is for the “*full*” (unfiltered) dataset.

### 2.1.2 Improving convergence in reciprocal space for DFT calculations

The DFT calculations in ODAC23 used a  $1 \times 1 \times 1$  k-point sampling for all MOFs, which can potentially cause numerical convergence issues for MOFs with small unit cells. A more accurate approach is to set the number of k-points to  $\lceil K/a \rceil \times \lceil K/b \rceil \times \lceil K/c \rceil$  for a unit cell of size  $a \times b \times c$  for a suitably large k-point density,  $K$ . Figure S1a shows the k-point convergence for 100 randomly selected systems from ODAC23. Around 7% of the calculations with the ODAC23 settings have noticeable systematic errors ( $> 0.2$  eV) as compared to  $K = 40 \text{ \AA}$ , but the errors are negligible by  $K = 40 \text{ \AA}$ .

Re-running full DFT relaxations at a higher k-point density is computationally expensive, as each relaxation trajectory contains hundreds of frames. We instead use a simple method to upgrade calculations to approximately match higher k-point density calculations at a significantly reduced cost. Numerical tests confirmed the expectation that energy errors due to low k-point density remain nearly constant across all frames within a trajectory (figure S1b). Given this observation, we can upgrade the calculations by calculating the energy errors of the initial and final frames and using the average of these two errors to correct for the energies of all frames in the trajectory. Figure S1b shows that applying this correction reduces convergence errors in total energy by an order of magnitude, to  $\sim 0.01$  eV. Since the average trajectory consists of over 200 frames, this procedure incurs less than 1% of the computational cost of naively re-running each frame. We did not apply these corrections to forces because we found the force errors to be very small ( $\sim 0.01$  eV/ $\text{\AA}$ ).

### 2.1.3 Re-relaxations of empty MOFs

Nearly all previous HTCS studies of MOFs approximated MOF structures as being rigid. By performing DFT relaxation for a large number of MOFs, ODAC23 provided interesting insight into the influence of adsorbed molecules on MOF structures. Although the presence of adsorbates causes (typically local) deformation in MOFs, it might be expected that removing the adsorbate and re-relaxing the MOF would lead to the same structure as the original empty MOF. In the ODAC23 dataset, however, we found many instances where this kind of re-relaxation yields a more energetically favorable empty MOF than the original structure due to perturbations and broken symmetries induced by the adsorbate. The energy of the

empty MOF is an important quantity in computing molecular adsorption energies, so failure to use the correct ground state empty MOF can cause significant artifacts in the adsorption energies [30, 34].

To address this effect, we re-relaxed empty MOFs after every converged MOF+adsorbate DFT relaxation in ODAC25. Because we typically sampled multiple adsorbate identities and placements in each MOF, these re-relaxations potentially generated more than one structure for each MOF. In all calculations below that require a reference energy for an empty MOF, the lowest energy structure among the available collection of re-relaxed MOFs is used. The effect of this approach for the MOFs included in ODAC23 is shown in [figure 2](#), which shows the energy differences between the most favorable empty MOF geometry in ODAC25 ( $E_{ground}$ ) and the original DFT-relaxed empty MOF in ODAC23 ( $E_{empty}$ ). These energies both correspond to local minima as determined by DFT.  $E_{ground}$  is determined from the minimum energy MOF configuration resulting from adsorption of  $N_2$  and  $O_2$ , as discussed in [section 2.2.1](#), or from any combination of  $CO_2$  and  $H_2O$  used in ODAC23 (i.e., lone  $CO_2$ , lone  $H_2O$ ,  $CO_2+H_2O$ , and  $CO_2+2H_2O$ ). There are many MOFs where this energy difference is non-trivial. In ODAC25, we corrected all ODAC23 adsorption energies and performed all additional calculations ([section 2.2](#)) using this method. Our ODAC25 adsorption energy calculations featuring this method supersede those presented in ODAC23. We note that for calculations that rely on total energies such as the training of MLFFs, all of the distinct local minima obtained by DFT for a given structure are useful. This re-relaxation approach is only necessary to calculate physically relevant adsorption energies.

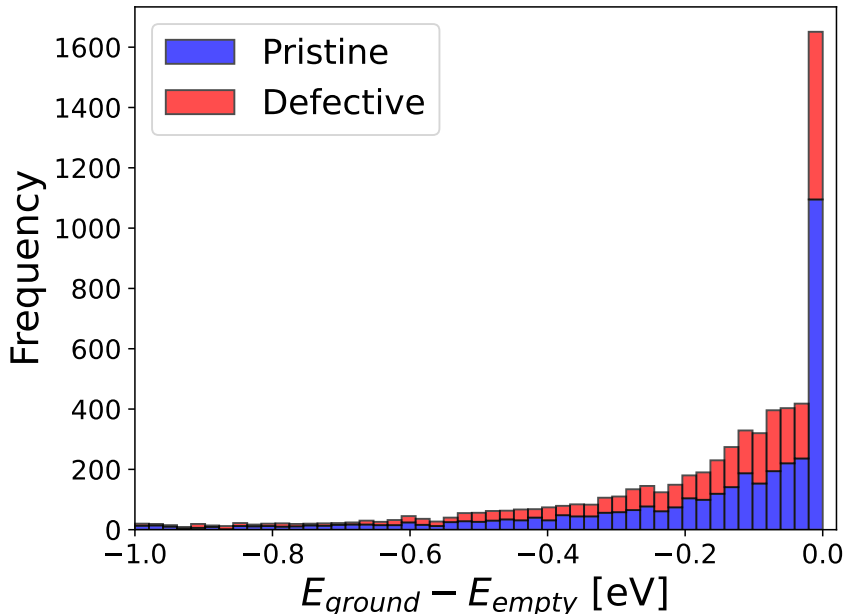


**Figure 2** Comparison of original DFT-relaxed empty MOF energies ( $E_{empty}$ ) to the most favorable MOF energy found across all ODAC25 relaxations ( $E_{ground}$ ) for 3,592 pristine and 2,788 defective ODAC23 MOFs.

[Figure S2](#) shows the distributions of ODAC23 adsorption energies and their corresponding ODAC25 adsorption energies corrected using MOF re-relaxations. The adsorption energies

after accounting for re-relaxation (orange data in [figure S2](#)) are shifted towards less favorable adsorption than the adsorption energies reported with ODAC23 (blue data). The adsorption energy median shift is  $> 0.1$  eV for all splits. Nevertheless, there are many examples in which the adsorption energy for individual  $\text{CO}_2$  or  $\text{H}_2\text{O}$  molecules is chemisorption-like (that is, more favorable than  $-0.5$  eV). Using the minimum MOF energy in this manner is the physically relevant quantity, and ODAC25 adsorption energies should be used instead of the ODAC23 energies. We note that in some cases, the MOF configuration of the MOF+adsorbate will differ from the MOF configuration of the minimum energy MOF. In these cases, other more favorable adsorption sites are likely to exist, but are not necessarily sampled in the ODAC25 dataset.

## 2.2 Diversity of Adsorbates, Adsorbents, and Energetics

### 2.2.1 New adsorbates: $\text{N}_2$ and $\text{O}_2$

ODAC25 includes two new adsorbates,  $\text{N}_2$  and  $\text{O}_2$ , to enhance the dataset’s coverage of situations relevant to modeling DAC. We used the same adsorbate placement strategy as in ODAC23. That is, adsorbates are placed within the DFT-relaxed MOF unit cells using Monte Carlo sampling with classical force fields to identify diverse, energetically favorable configurations, then relaxed using DFT in calculations that allow all atoms to move with the PBE+D3 functional. ODAC25 contains nearly 56K  $\text{N}_2$  and  $\text{O}_2$  relaxation trajectories across  $\sim 6,400$  pristine and defective ODAC23 MOFs. [Figure S3](#) summarizes the  $\text{N}_2$  and  $\text{O}_2$  adsorption energy results.

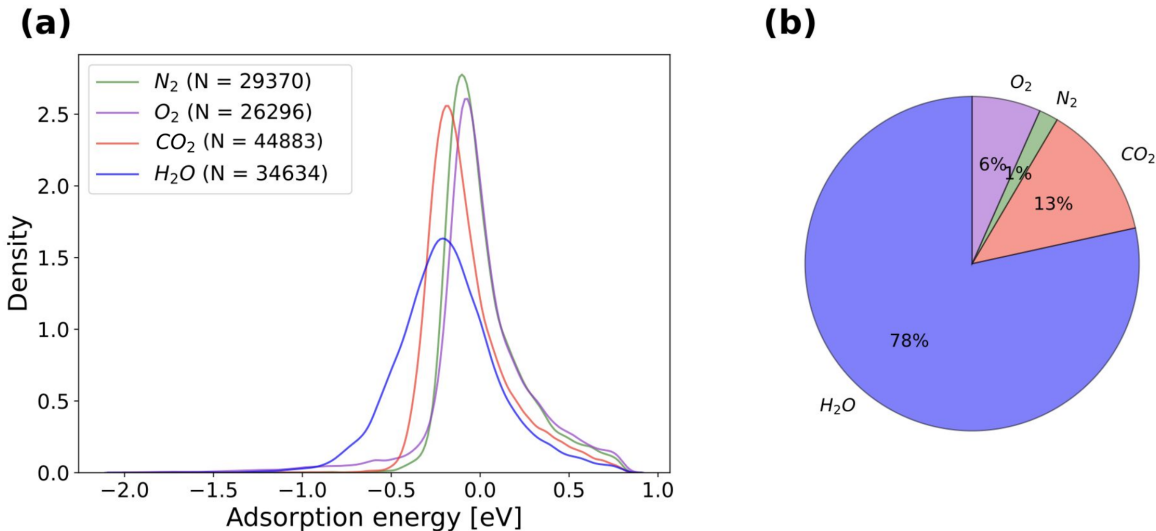


**Figure 3** (a) Distribution of adsorption energies for different adsorbates computed using kernel density estimation. (b) Percentage of MOFs that adsorb each adsorbate most strongly, determined by taking the strongest adsorption energy of each adsorbate across all sampled active sites in a given MOF framework.

The inclusion of multiple adsorbates with our DFT calculations can provide information about effects including competitive adsorption, redox activity, and the impact of  $\text{O}_2$  reactivity on

CO<sub>2</sub> adsorption sites. [Figure 3a](#) shows the distribution of binding energies from each DFT-relaxed configuration with a single adsorbed molecule (referenced to the most energetically favorable empty MOF structure available, as described above). [Figure S5](#) shows the histogram corresponding to the kernel density plot in [figure 3a](#). Across the entire ODAC25 dataset for single-adsorbate configurations, 30.8% of the configurations have positive adsorption energies, meaning adsorption is not energetically favored, 63.5% of the structure have adsorption energies between -0.5 and 0 eV, corresponding to physisorption, and 5.7% (8,320 configurations) show stronger adsorption in the chemisorption regime.

[Figure 3b](#) shows the percentage of MOFs that bind most strongly to different adsorbates among the collection of configurations in our DFT calculations. In over 75% of MOFs, the strongest adsorption energy occurs with H<sub>2</sub>O, while only 13% favor CO<sub>2</sub>, a key property for DAC sorbents [17]. Interestingly, 6% of MOFs bind O<sub>2</sub> most strongly, likely due to O<sub>2</sub> dissociation or strong spin polarization [35]. Surprisingly, a small number of MOFs favor N<sub>2</sub>.

We find 167 ODAC23 MOFs where the strongest observed adsorption energy is with N<sub>2</sub>. A small number of example of metal-organic clusters exhibiting N<sub>2</sub> chemisorption have been reported previously [36–38]. Our calculations sampled only a small number of configurations for each molecule (typically 2-5), so some of these cases may stem from incomplete sampling of the full potential energy surface for adsorbates. A full exploration of selectivity requires the Widom insertion method as discussed in [section 3.2](#).

MOFs with narrow MOF unit cells may show strong N<sub>2</sub> adsorption energies due to a computational artifact. Narrow unit cells, defined here as those with a shortest dimension < 7 Å, can artificially boost the calculated adsorption energy due to strong interactions between adsorbate molecules in neighboring periodic images (see [figure S6](#)). Narrow unit cells affect calculated adsorption energies for all four adsorbate molecules, with 6 of the 73 chemisorption-like N<sub>2</sub> adsorption energies resulting from this phenomenon. 11% (1,046) of ODAC25 MOFs have a shortest unit cell dimension of <7 Å, and we recommend users approach these MOFs with caution. Unit cell vectors included in the dataset may be used to filter for MOFs with narrow unit cells.

### 2.2.2 New adsorbents: functionalized MOFs

To broaden the scope of MOFs included in our dataset, we generated new MOF structures using two MOF amine functionalization methods. We first used linker functionalization, which has been shown experimentally to enhance CO<sub>2</sub> adsorption [39–44]. We generated amine-functionalized MOFs using seven organic linkers with amine groups that were previously used in MOF synthesis (see [table S2](#)). Second, we generated structures using OMS functionalization with diamines in which one amine is bound to an open metal site, while the other remains exposed in the pore. Experimental studies on functionalized MOFs of the latter kind including MIL-101 [45, 46], Mg-dobdc [47–49], and M<sub>2</sub>(dobpdc) (M=Mg, Mn, Fe, Co, Zn) [50, 51] have demonstrated exceptional CO<sub>2</sub> capture ability, especially at low CO<sub>2</sub> partial pressures. We functionalized MOF structures with different concentrations of ten diamines ([table S3](#)), including primary, secondary, and tertiary amines.

We developed our MOF functionalization process in Python, building on a previous MOF

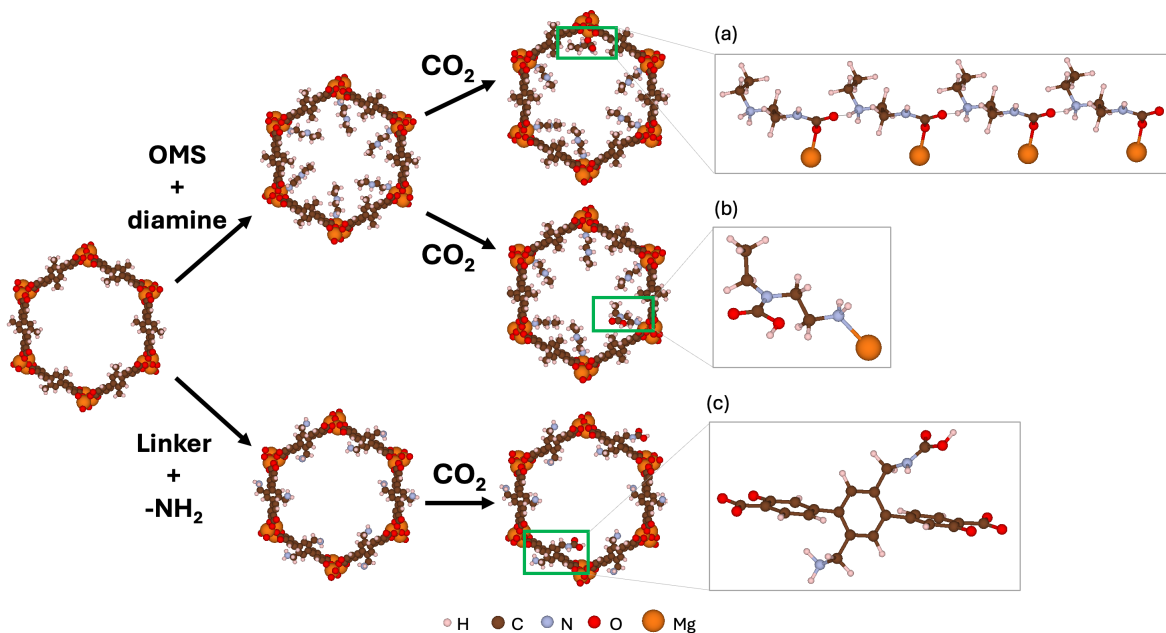


**Figure 4** Illustration of the two approaches used to generate configurations characteristic of reactive  $\text{CO}_2$  capture mechanisms in amine-functionalized MOFs, using IRMOF-74-III (CSD code RAVWAO) as an example. The OMS in this example were functionalized with een.

point defect generator [52]. An advantage of our approach is that it eliminates the need for user-specified substructures and instead automatically functionalizes MOFs using predefined methods. In addition, the package supports user-defined molecules for OMS functionalization.

We functionalized 110 pristine and 65 defective MOFs with  $\text{PLD} \geq 10 \text{ \AA}$  to allow enough space for amine groups and  $\text{CO}_2$  adsorption. During the linker functionalization process, we used MOFid [53] to separate metal centers and linkers. The separated linkers were then compared to the linker candidates in table S2. If a match was found, the corresponding modification was applied to the linker by adding amine functional groups. Original linkers were functionalized at all possible concentrations, with concentration defined as the number of sites modified relative to the total available sites. For OMS functionalization, we used the OMS detection algorithm developed in the CoRE MOF 2019 database [54]. If an OMS was detected in a MOF structure, diamines were grafted at all possible concentrations in the unit cell. All ten diamines in table S3 were used. In each case the more primary amine was appended to the OMS. The orientations of the diamines were pre-optimized to avoid overlapping atoms, then structures were DFT relaxed. This generated a total of 7,163 distinct DFT-relaxed amine-functionalized MOF structures. The PLDs of all functionalized MOFs were calculated after DFT relaxation, and only structures with  $\text{PLD} \geq 3.3 \text{ \AA}$  were subsequently used for adsorbate placement and DFT relaxation.

We used DFT to relax adsorbed  $\text{CO}_2$  and  $\text{H}_2\text{O}$  in all functionalized MOFs. We first used the ODAC23 strategy for the placement of  $[\text{CO}_2]$ ,  $[\text{H}_2\text{O}]$ ,  $[\text{1CO}_2+\text{1H}_2\text{O}]$  and  $[\text{1CO}_2+\text{2H}_2\text{O}]$  in all functionalized MOFs [12]. A limitation of this approach is that it relies on a classical FF that does not allow configurations corresponding to reactions between molecules and amine groups. If an energy barrier exists between these states and configurations involving reactions, DFT

relaxation from the initial state will not find the physically interesting latter state.

To address this limitation, we performed additional calculations specifically aimed at generating initial configurations similar to those known from CO<sub>2</sub> reactions with amines. We investigated two CO<sub>2</sub> reactive capture mechanisms involving amines. The first mechanism is the cooperative formation of ammonium carbamate [50, 51, 55–59]. CO<sub>2</sub> inserts into each metal amine bond, forming ion-paired ammonium carbamate chains (illustrated in [figure 4a](#)). This mechanism has been studied in detail previously in a DFT climbing-image nudged elastic band (CI-NEB) study in mmen-Mg<sub>2</sub>(dobpdc) [60].

We also generated initial states involving carbamic acid as shown in [figure 4b](#). Compared with 2:1 amine:CO<sub>2</sub> stoichiometry for the mechanism generating ammonium carbamate, this represents a 1:1 amine:CO<sub>2</sub> stoichiometry. Carbamic acids have been experimentally identified in CO<sub>2</sub> capture using post-synthesized OMS amine functionalized MOFs [57, 61]. For MOFs with linker functionalization, CO<sub>2</sub> reacts with the amine groups on the linker to form the carbamic acid ([figure 4c](#)). This mechanism has been observed experimentally using NMR in the linker-functionalized IRMOF-74-III-CH<sub>2</sub>NH<sub>2</sub> [40] and IRMOF-74-III-(CH<sub>2</sub>NH<sub>2</sub>)<sub>2</sub> [39].

For linker functionalized MOFs, one random functionalized amine group (–NH<sub>2</sub>) was selected and replaced with carbamic acid group (–NHCOOH). For OMS functionalization, one random grafted diamine was selected and replaced with corresponding ammonium (NR<sub>3</sub>H<sup>+</sup>) and carbamate (NR<sub>2</sub>COO<sup>–</sup>), or carbamic acid NR<sub>2</sub>COOH if the outer amine was primary or secondary, respectively. For each functionalized MOF with 1 CO<sub>2</sub> placed using one of the reactive placements outlined above, we also created structures with 1 and 2 H<sub>2</sub>O to generate functionalized structures with [1CO<sub>2</sub>+1H<sub>2</sub>O] and [1CO<sub>2</sub>+2H<sub>2</sub>O]. In total, we successfully generated 52,756 adsorbate placements in 3,920 functionalized MOFs. Automated generation of functionalized MOFs is challenging, and some of our structures may not be experimentally relevant or accessible, but all of the included structures correspond to converted DFT calculations and provide additional diversity to the dataset.

It is interesting to compare CO<sub>2</sub> and H<sub>2</sub>O adsorption energies in MOFs with and without functionalization. For each bare MOF, there exists an ensemble of functionalized MOFs, each with several CO<sub>2</sub> and H<sub>2</sub>O placements. We considered MOFs with data for adsorption of a single CO<sub>2</sub> and a single H<sub>2</sub>O in both the non-functionalized base MOF and at least one functionalized MOF for this analysis, and we excluded cases corresponding to H<sub>2</sub>O adsorption in functionalized MOFs generated by the reactive methods defined above. This gave data from 2,093 functionalized MOFs derived from 73 CoRE MOFs, with a total of 12,065 and 10,049 CO<sub>2</sub> and H<sub>2</sub>O adsorption energies in the functionalized MOFs, respectively. Notably, the reference energies for empty functionalized MOFs most often result from MOF + H<sub>2</sub>O configurations since the MOFs do not deform enough in the presence of CO<sub>2</sub> to approach the most energetically favorable empty MOF configurations (see [figure S4](#)). This causes many of the resulting CO<sub>2</sub> adsorption energies to be positive.

[Figure 5a](#) compares the most favorable CO<sub>2</sub> and H<sub>2</sub>O adsorption energies from the non-functionalized MOFs to the functionalized MOFs described above. Functionalization in general makes adsorption more favorable, as expected, with roughly equal effects on CO<sub>2</sub> and H<sub>2</sub>O adsorption energies. [Figure 5b](#) compares the adsorption energy distributions in linker-functionalized MOFs relative to OMS-functionalized MOFs. The CO<sub>2</sub> adsorption

energies are broadly similar in the two types of functionalized MOFs, which differs from existing literature showing weaker adsorption energies in linker-functionalized MOFs ( $-0.3$  to  $-0.4$  eV) relative to OMS-functionalized MOFs ( $-0.6$  to  $-0.9$  eV) [62]. Figure S7 shows the histogram corresponding to the kernel density plot in figure 5b. For OMS-functionalized MOFs, figure S8 shows the adsorption energy distributions in MOFs functionalized with each diamine, and figure S9 shows the  $\text{CO}_2$  adsorption energies in OMS-functionalized MOFs as a function of diamine concentration. There is minimal correlation between diamine type, diamine concentration, and adsorption energies in our data because our adsorbate placement method did not guarantee placement near functionalized linkers or OMSs. Further analysis, including careful treatment of adsorbate placements, is needed to draw detailed conclusions about the effects of functionalization, and is outside the scope of this work.

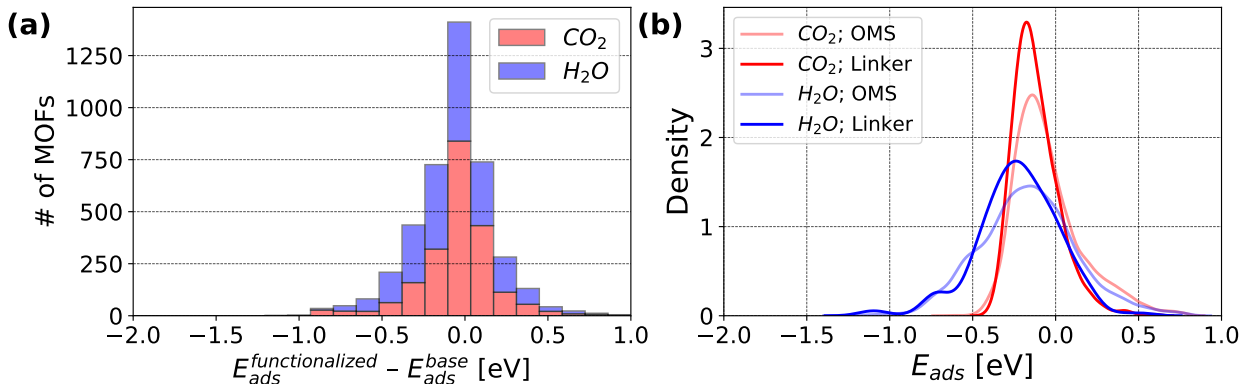


**Figure 5** (a) Difference in most favorable adsorption energies between functionalized MOFs and their corresponding base MOFs. (b) Kernel density estimation plots for all  $\text{CO}_2$  and  $\text{H}_2\text{O}$  adsorption energies in linker-functionalized ( $N = 147$ ) and OMS-functionalized ( $N = 2,672$ ) MOFs. There are 672  $\text{CO}_2$  and 577  $\text{H}_2\text{O}$  adsorption energies and 11,395  $\text{CO}_2$  and 9,472  $\text{H}_2\text{O}$  adsorption energies in linker- and OMS-functionalized MOFs, respectively.

### 2.2.3 High-energy configurations from GCMC

To further enhance the diversity of training data in ODAC25, we included DFT energies for adsorption configurations not at local energy minima generated via Grand Canonical Monte Carlo (GCMC) simulations. These configurations were generated using the RASPA package with classical force fields, employing the Universal Force Field (UFF) for the MOF frameworks and holding the MOF rigid in its initial DFT-relaxed structure from ODAC23. The GCMC calculations were performed for all pristine and defective MOFs in the ODAC23 dataset, covering a wide range of pressure, composition, and molecular interaction scenarios.

GCMC simulations were run at 300 K for pressures of 5, 10, 20, and 50 kPa. To explore mixed-component adsorption behavior, we performed simulations with pure  $\text{CO}_2$  and pure  $\text{H}_2\text{O}$  and mixtures with  $\text{CO}_2$ - $\text{H}_2\text{O}$  gas phase molar ratios of 1:1, 1:5, 1:10, and 1:20. Because adsorption in MOFs is selective (typically for  $\text{H}_2\text{O}$  relative to  $\text{CO}_2$ ) this approach generates a wide range of adsorbed compositions. Each simulation was run for 500,000 steps.

From these GCMC simulations, random intermediate configurations were saved and single-point DFT calculations were performed (without energy minimization) to compute energies

and forces. With this approach, we generated over 2.7 million single-point DFT calculations. [Figure S10](#) shows a histogram of the number of CO<sub>2</sub> and H<sub>2</sub>O molecules in this data split. This large collection of DFT expands the data set in two important ways relevant for accurately predicting adsorption isotherms: inclusion of states with large numbers of adsorbed molecules and states that may differ considerably from adsorption in energy-minimized adsorption sites.

#### 2.2.4 Synthetically generated MOFs

We further increased the diversity of ODAC25 by including 460 synthetically generated MOFs. To this end, we generated 53,000 candidate structures with CuspAI’s in-house generative model of MOFs. An autoregressive transformer model samples MOF specifications in the form of a sequence of the topology, the identities of the metal clusters, and the identities of the ligands. We assemble these specifications into atomistic structures using Pormake [\[63\]](#).

The generated structures were initially optimized with the UFF4MOF force field [\[16\]](#). This relaxation protocol includes a phase of MD simulation at room temperature, and we rejected structures in which the unit cell explodes or collapses. MOFChecker v0.9.6 [\[30\]](#) was used to screen the structures for overlapping atoms and improper metal coordination as described in [section 2.1.1](#). In addition to rejecting problematic structures flagged by MOFChecker, we excluded structures with more than 250 atoms in the unit cell, PLDs less than 3.64 Å or more than 20 Å, and structures containing lanthanides or actinides.

Of the remaining 4000 structures, we selected the 460 that improve the diversity of ODAC25 the most. We use farthest point sampling [\[64\]](#) in a space that combines several features that characterize MOFs, including geometric properties related to porosity and surface area, autocorrelation functions [\[65\]](#), as well as the heat of adsorption of CO<sub>2</sub>. We compute these features with mofdscribe [\[66\]](#), RASPA [\[67\]](#), and Zeo++ [\[68\]](#).

The selected structures were relaxed with DFT. For the limited number of structures for which this relaxation failed, the structures were removed and replaced with new candidates, again using farthest point sampling approach. [Figure S11](#) shows that the resulting hypothetical structures successfully extend the space covered by ODAC25 toward more complex geometries featuring larger pores, higher surface areas, and lower densities compared to experimental structures. [Figure S12](#) shows the distributions of CO<sub>2</sub>, H<sub>2</sub>O, N<sub>2</sub>, and O<sub>2</sub> adsorption energies in these synthetic MOFs. Configurations with multiple (up to 15) adsorbate molecules are excluded from [figure S12](#).

### 3 Results: ML Interatomic Potentials

The development of machine learned interatomic potentials (MLIP) has seen rapid progress over the last few years, and various architectures have been developed for molecules and materials [\[27, 69–75\]](#). More recently, a number of foundational MLIPs trained on multiple datasets across different classes of materials and molecules have been developed, demonstrating that a single model can accurately predict energies and forces across different chemical modalities [\[29, 75\]](#). The ODAC23 paper demonstrated that state-of-the-art MLIPs trained on adsorption energies and forces from the ODAC23 dataset significantly outperformed classical

force fields based on UFF, particularly in the chemisorption regime.

### 3.1 Adsorption Energy and Force Evaluations

In this section, we describe the results recent MLIPs trained on the ODAC25 dataset on the *Structure to Energy and Forces (S2EF)* task, which involves predicting the non-relaxed adsorption energy and atomic forces. This is analogous to evaluating a force field. Our experiments use two recent model architectures: eSEN [28], and UMA [29]. Our training setup is similar to the ODAC23 models. All models were trained to optimize the following objective:

$$\mathcal{L} = \lambda_E \sum_i |\hat{E}_i - E_i| + \lambda_F \sum_{i,j} \frac{1}{3N_i} |\hat{F}_{ij} - F_{ij}|^2 \quad (1)$$

where  $E_i$  and  $\hat{E}_i$  are, respectively, the ground truth and predicted energies of system  $i$  with  $N_i$  atoms, and  $F_{ij}$  and  $\hat{F}_{ij}$  are, respectively, the ground truth and predicted forces for the  $j$ -th atom in system  $i$ . The loss coefficients  $\lambda_E$  and  $\lambda_F$  are hyperparameters used to trade-off the force and energy losses. For each model, we use the same model sizes that were originally published, but we tune the learning rate and the loss coefficients.

Unlike ODAC23 models which were trained to directly predict the adsorption energy, we use the total DFT energy (with the k-point corrections described in section 2.1.2) as the energy target for training our models. This follows the suggestion by Abdelmaqsoud et al. [76] that total energy models can better handle surface reconstructions. To improve training stability and convergence, we apply a linear reference to these energies using the same protocol that was used in the OC22 paper [77]. Once trained, the adsorption energy can be calculated by subtracting the energies of the lowest-energy bare MOF and energies of adsorbates from the energy of the combined MOF-adsorbate system:

$$\hat{E}_{\text{ads}} = \hat{E}_{\text{system}}(r_{\text{system}}) - \hat{E}_{\text{MOF}}(r_{\text{system}}) - \sum_{\text{adsorbate}} E_{\text{adsorbate}}(r_{\text{adsorbate}}) \quad (2)$$

where  $\hat{E}_{\text{system}}(r_{\text{system}})$  is the predicted energy of the combined MOF-adsorbate system,  $\hat{E}_{\text{MOF}}$  is the energy of the lowest energy bare configuration of the corresponding MOF (as described in section 2.1.3), and  $E_{\text{adsorbate}}(r_{\text{adsorbate}})$  is the energy of a single adsorbate in the gas phase. The summation is performed over all adsorbates. In our model evaluation, we compare the adsorption energy predicted by various MLIPs with the adsorption energies derived from DFT calculations.

Table 1 shows the results on S2EF task for various models. The UMA-Small model [29] extends the eSEN architecture using mixture of linear experts (MOLE) that enables increasing model capacity without sacrificing speed. It was trained on a subset of ODAC25 with carbon dioxide and water adsorbates (without functionalized MOFs), jointly with a number of other datasets spanning various molecules and materials. The two eSEN models, based on the architecture from Fu et al. [28], were trained on the full ODAC25 dataset and the filtered ODAC25 dataset respectively. All of these models implement rotational equivariance, a property that has

**Table 1** Overall performance of various models on the S2EF task across all adsorbates. Total Energy MAE (EMAE-Tot) and Adsorption Energy MAE (EMAE) are reported in eV, and Force MAE (FMAE) is reported in eV/Å. The best result in each column is shown in bold font.

Model	Training Set	EMAE-Tot↓	EMAE↓	FMAE↓
EquiformerV2 large [12]	ODAC23	–	0.155	0.024
MACE [78]	MPtraj [79]	–	0.323	0.369
MACE-DAC [80]	MPtraj [79]+GoldDAC	–	0.222	0.289
UMA-Small 1.1 [81]	ODAC25 subset+others	0.282	0.110	0.040
eSEN (Full)	ODAC25-Full	<b>0.195</b>	<b>0.077</b>	<b>0.023</b>
eSEN (Filtered)	ODAC25-Filtered	0.268	0.080	0.033

**Table 2** Performance breakdown of various models on the S2EF task by individual adsorbate configurations. Adsorption Energy MAE (EMAE) is reported in eV and Force MAE (FMAE) is reported in eV/Å. The UMA model was trained on a subset of ODAC25, while the two eSEN models were trained on the full and filtered versions of ODAC25. The best result in each column is shown in bold font.

Model	CO <sub>2</sub>		H <sub>2</sub> O		CO <sub>2</sub> +H <sub>2</sub> O		N <sub>2</sub>		O <sub>2</sub>	
	EMAE↓	FMAE↓	EMAE↓	FMAE↓	EMAE↓	FMAE↓	EMAE↓	FMAE↓	EMAE↓	FMAE↓
EquiformerV2 large[12]	0.117	0.025	0.232	0.025	0.129	<b>0.024</b>	0.219	0.036	0.242	0.048
MACE [78]	0.219	0.382	0.168	0.392	0.367	0.355	0.550	0.420	0.209	0.456
MACE-DAC [80]	0.106	0.301	0.149	0.317	0.252	0.272	0.380	0.322	0.284	0.368
UMA-Small 1.1 [81]	0.074	0.041	0.082	0.042	0.103	0.037	0.386	0.044	0.157	0.060
eSEN (Full)	<b>0.061</b>	<b>0.024</b>	0.075	<b>0.022</b>	<b>0.081</b>	<b>0.024</b>	<b>0.081</b>	<b>0.028</b>	<b>0.068</b>	<b>0.044</b>
eSEN (Filtered)	0.063	0.033	<b>0.070</b>	0.028	0.085	0.034	0.093	0.037	0.080	0.064

been shown to improve MLIP performance. They also constrain their predicted forces to be energy conserving by predicting the forces as a gradient of their predicted energies. Since this gradient computation is expensive and requires a large amount of GPU memory, these models are trained in two stages. In the first, *pre-training* stage, the models are trained to directly predict forces without enforcing energy conservation. In the final, *fine-tuning* stage, the models are further trained on a subset of the training data with the energy conserving property enforced. The full set of model hyperparameters are provided in the SI [appendix J](#).

For comparison, we include EquiformerV2-Large trained on ODAC23 data, the best performing model from the ODAC23 paper, MACE [75] a recent foundation model, and MACE-DAC [80], a version of MACE that was fine-tuned to model CO<sub>2</sub> and H<sub>2</sub>O interactions in MOFs using the GoldDAC dataset. EquiformerV2-Large is based on the EquiformerV2 [27] architecture, an equivariant graph neural network, and contains 153M parameters. It was trained to predict interaction energies directly on the ODAC23 dataset.

[Table 1](#) shows the results of all models on the S2EF task for the MOF + Adsorbate test set of the filtered ODAC25 dataset. Models trained on ODAC25 significantly outperform prior models. The eSEN models trained on the filtered and full ODAC25 datasets achieve the best overall results with energy MAEs of 0.085 eV and 0.077 eV, and force MAEs of 0.032 eV/Å and 0.023 eV/Å respectively. The UMA-Small model, trained on a subset of

ODAC25 along with other datasets, shows strong performance with energy MAE of 0.110 eV and a force MAE of 0.040 eV/Å. Table 2 breaks down the metrics for each adsorbate type. The eSEN models achieve lower energy and force MAEs on all metrics. The UMA-Small model is competitive to the eSEN models on CO<sub>2</sub> and H<sub>2</sub>O, but shows degraded performance for the adsorbates it was not trained on. These results confirm that ODAC25 provides a strong foundation for training MLIPs that generalize across a wide range of MOF–adsorbate configurations and energies.

### 3.2 Widom Insertion and Henry’s Coefficients

To further evaluate the accuracy of various MLIPs, we calculated Henry’s coefficients for CO<sub>2</sub> and N<sub>2</sub> in several MOFs. The Henry coefficient ( $K_H$ ) is the slope of an adsorbate’s isotherm in the low-loading limit. The ratio of Henry’s coefficients for two adsorbates gives the adsorption selectivity for the molecular pair in the low loading limit, and this selectivity is often representative of adsorption performance over a wide range of pressures [82].

Computationally, we calculate Henry’s coefficients using the Widom insertion method [83]. This method involves randomly inserting test molecules into the rigid MOF structure and computing their interaction energy. We approximated the MOF as being rigid in these calculations, so the MOF-adsorbate interaction energy is given by Eq. 2. The Henry’s coefficient is then calculated as:

$$K_H = \frac{\beta}{V} \langle \exp(-\beta \hat{E}_{\text{int}}) \rangle$$

where  $\beta = 1/k_B T$ ,  $V$  is the system volume, and the angle brackets denote an expectation value over uniformly distributed insertion positions and orientations [84]. Because the Henry’s coefficient averages over the entire pore structure, it represents an example of using force fields to compute a property that cannot be assessed from a small collection of DFT calculations.

As a baseline, we perform these calculations using the Universal Force Field (UFF) [85] as implemented in the RASPA2 simulation package [67] with the Automated Interactive Infrastructure and Database for Computational Science (AiiDA) framework [86]. The baseline uses the Transferable Potentials for Phase Equilibria (TraPPE) force field [87] for the CO<sub>2</sub> and N<sub>2</sub> molecules. To evaluate the MLIPs introduced in this paper, we employ a Python package<sup>1</sup> based on DAC-SIM [80] that can perform Widom insertion calculations with any Atomic Simulation Environment (ASE) [88] calculator. This allows us to directly compare the performance of different MLIPs against the UFF baseline.

Our benchmark dataset consists of several well-known MOF structures (UiO-66, HKUST-1, MOF-5) from the curated experimental dataset published in [89]. Multiple independent experimental isotherms are available for each of these materials [90]. These materials are expected to only involve physisorption, where the rigid framework assumption used in our Widom insertion calculations is likely to be reasonable.

We compare the computational value to experimental Henry’s coefficients, which were extracted by fitting the first two data points of the published isotherms to a line passing through the

---

<sup>1</sup>Released at <https://github.com/Cusp-AI/widom>

origin. When multiple isotherms are available for the same MOF, gas and temperature, we averaged the Henry coefficient.

**Table 3** Errors of Henry coefficient prediction for different models on CO<sub>2</sub> and N<sub>2</sub>. We show the mean absolute error between predictions and experimental values in eV, which is proportional to the logarithm of the Henry’s constant [84]. The best result in each column is shown in bold font.

Model	Training Set	CO <sub>2</sub>	N <sub>2</sub>
UFF	-	0.0299	0.0190
MACE-MP-0b2 [78]	MPtraj [79]	0.0566	0.0448
MACE-DAC [80]	MPtraj [79] + GoldDAC	0.0513	0.0698
UMA-Small 1.1 [81]	ODAC25 subset + others	0.0274	0.0631
UMA-Medium 1.1 [81]	ODAC25 subset + others	<b>0.0145</b>	0.0286
eSEN	ODAC25-Full	0.0250	0.0433
eSEN	ODAC25-Filtered	0.0234	<b>0.0136</b>

Table 3 shows the results for Henry coefficient predictions across different models for CO<sub>2</sub> and N<sub>2</sub> adsorbates. For both CO<sub>2</sub> and N<sub>2</sub>, we see that the best performing model is the one trained on more CO<sub>2</sub> and N<sub>2</sub> data, respectively. For CO<sub>2</sub> adsorption, all ODAC25 models outperform the UFF baseline, while the MACE foundation model and the specialized MACE-DAC perform substantially worse. Of the ODAC25 models, the largest, UMA-Medium 1.1, performs best. For N<sub>2</sub> adsorption, the UMA models, which were not trained on N<sub>2</sub>, as well as the MACE models, do not surpass the UFF baseline, while the eSEN model trained on the filtered ODAC25 data performs best. Scatter plots of the experimental and predicted values are shown in figure S13. Methods exist for incorporating MOF flexibility into computation of Henry’s coefficients and adsorption isotherms when force fields are available for the MOF degrees of freedom [91], so an interesting future direction will be to adapt these methods for use with MILPs.

## 4 Conclusion

The ODAC25 dataset represents a significant step forward in computational sorbent discovery for direct air capture (DAC). Building upon the foundation laid by ODAC23, this expanded dataset addresses critical gaps in DFT calculation accuracy and chemical diversity. ODAC25 improves chemical validation of MOFs and k-point sampling during DFT calculations. Systematic errors in adsorption energies caused by adsorbate-induced MOF deformation are treated using a physically relevant approach. ODAC25 expands upon the diversity of ODAC23 by introducing N<sub>2</sub> and O<sub>2</sub> as adsorbates, exploring the potential of functionalized and synthetically generated MOFs, and incorporating high-energy configurations generated from GCMC simulations. These additions provide a more comprehensive understanding of competitive adsorption and multicomponent interactions, which are essential for modeling realistic air separations.

By leveraging advanced data generation methodologies, ODAC25 captures a diverse range of adsorption phenomena, from single-molecule chemisorption to complex multicomponent

configurations. The integration of Grand Canonical Monte Carlo (GCMC) data, paired with single-point DFT calculations, bridges the gap between atomistic modeling and process-level predictions, enhancing the dataset’s relevance to both high-throughput screening and machine learning model training.

The updated machine learning force fields, trained on the expanded dataset, demonstrate improved performance on both ODAC23 test sets and new functionalized MOFs, highlighting the value of the extended data. These models advance the field by better capturing complex interactions and enabling accurate predictions across a wider range of sorbent chemistries and conditions.

ODAC25 not only expands the chemical and configurational space explored for DAC but also sets the stage for further advancements in computational sorbent design. Future work will focus on incorporating more advanced isotherm predictions, integrating process modeling, and conducting lifecycle analyses to evaluate the environmental and economic impact of DAC technologies. By making the dataset, models, and tools publicly available, we aim to empower the community to accelerate the development of scalable and energy-efficient sorbents for carbon dioxide removal.

## 5 Acknowledgment

We acknowledge Jin, Garcia, and Smit [26] for their correspondence on the ODAC23 dataset, and for helpful discussions, which highlighted important considerations regarding “charged” MOF structures and binding energy calculation methodologies. Their feedback has informed improvements in the ODAC25 dataset, including enhanced structure validation and systematic corrections for MOF re-relaxation effects discussed in [section 2](#).

## References

- [1] A. Sood and S. Vyas, “Carbon Capture and Sequestration- A Review,” in *IOP Conference Series: Earth and Environmental Science*, vol. 83, no. 1. Institute of Physics Publishing, 9 2017.
- [2] E. S. Sanz-Pérez, C. R. Murdock, S. A. Didas, and C. W. Jones, “Direct capture of CO<sub>2</sub> from ambient air,” *Chem. Rev.*, vol. 116, no. 19, pp. 11 840–11 876, Aug. 2016. [Online]. Available: <https://doi.org/10.1021/acs.chemrev.6b00173>
- [3] T. Tiainen, J. K. Mannisto, H. Tenhu, and S. Hietala, “CO<sub>2</sub> Capture and Low-Temperature Release by Poly(aminoethyl methacrylate) and Derivatives,” *Langmuir*, vol. 38, no. 17, pp. 5197–5208, 5 2022.
- [4] H. Furukawa, K. E. Cordova, M. O’Keefe, and O. M. Yaghi, “The chemistry and applications of metal-organic frameworks,” *Science*, vol. 341, p. 1230444, 2013.
- [5] A. M. P. Peedikakkal and I. H. Aljundi, “Mixed-Metal Cu-BTC Metal-Organic Frameworks as a Strong Adsorbent for Molecular Hydrogen at Low Temperatures,” *ACS Omega*, vol. 5, no. 44, pp. 28 493–28 499, 11 2020.
- [6] S. Jamdade, R. Gurnani, H. Fang, S. E. Boulfefel, R. Ramprasad, and D. S. Sholl, “Identifying High-Performance Metal-Organic Frameworks for Low-Temperature Oxygen Recovery from Helium by Computational Screening,” *Industrial and Engineering Chemistry Research*, vol. 62, no. 4, pp. 1927–1935, 2 2023.
- [7] S. M. Moosavi, A. Chidambaram, L. Talirz, M. Haranczyk, K. C. Stylianou, and B. Smit, “Capturing chemical intuition in synthesis of metal-organic frameworks,” *Nature Communications*, vol. 10, no. 1, 12 2019.
- [8] S. M. Moosavi, A. Nandy, K. M. Jablonka, D. Ongari, J. P. Janet, P. G. Boyd, Y. Lee, B. Smit, and H. J. Kulik, “Understanding the diversity of the metal-organic framework ecosystem,” *Nature Communications*, vol. 11, no. 1, 12 2020.
- [9] N. Stock and S. Biswas, “Synthesis of metal-organic frameworks (mofs): Routes to various mof topologies, morphologies, and composites,” *Chemical Reviews*, vol. 112, no. 2, pp. 933–969, 2012, pMID: 22098087. [Online]. Available: <https://doi.org/10.1021/cr200304e>
- [10] H. Daglar and S. Keskin, “Recent advances, opportunities, and challenges in high-throughput computational screening of MOFs for gas separations,” *Coordination Chemistry Reviews*, vol. 422, 11 2020.
- [11] C. E. Wilmer, M. Leaf, C. Y. Lee, O. K. Farha, B. G. Hauser, J. T. Hupp, and R. Q. Snurr, “Large-scale screening of hypothetical metal-organic frameworks,” *Nature Chemistry*, vol. 4, no. 2, pp. 83–89, 2 2012.
- [12] A. Sriram, S. Choi, X. Yu, L. M. Brabson, A. Das, Z. Ulissi, M. Uyttendaele, A. J. Medford, and D. S. Sholl, “The Open DAC 2023 dataset and challenges for sorbent discovery in direct air capture,” *ACS Central Science*, vol. 10, no. 5, pp. 923–941, 2024. [Online]. Available: <https://doi.org/10.1021/acscentsci.3c01629>
- [13] J. A. Harrison, J. D. Schall, S. Maskey, P. T. Mikulski, M. T. Knippenberg, and B. H. Morrow,

- “Review of force fields and intermolecular potentials used in atomistic computational materials research,” *Applied Physics Reviews*, vol. 5, no. 3, 9 2018.
- [14] A. Rappé, C. Casewit, K. Colwell, W. Goddard III, and W. Skiff, “UFF, a Full Periodic Table Force Field for Molecular Mechanics and Molecular Dynamics Simulations,” *Journal of American Chemical Society*, vol. 114, no. 28, p. 631, 1992. [Online]. Available: <https://pubs.acs.org/sharingguidelines>
- [15] M. A. Addicoat, N. Vankova, I. F. Akter, and T. Heine, “Extension of the universal force field to metal-organic frameworks,” *Journal of Chemical Theory and Computation*, vol. 10, no. 2, pp. 880–891, 2 2014.
- [16] D. E. Coupry, M. A. Addicoat, and T. Heine, “Extension of the Universal Force Field for Metal-Organic Frameworks,” *Journal of Chemical Theory and Computation*, vol. 12, no. 10, pp. 5215–5225, 10 2016.
- [17] J. M. Findley and D. S. Sholl, “Computational Screening of MOFs and Zeolites for Direct Air Capture of Carbon Dioxide under Humid Conditions,” *Journal of Physical Chemistry C*, vol. 125, no. 44, pp. 24 630–24 639, 11 2021.
- [18] Y. J. Colón and R. Q. Snurr, “High-throughput computational screening of metal-organic frameworks,” *Chemical Society Reviews*, vol. 43, no. 16, pp. 5735–5749, 8 2014.
- [19] S. Lee, B. Kim, H. Cho, H. Lee, S. Y. Lee, E. S. Cho, and J. Kim, “Computational Screening of Trillions of Metal-Organic Frameworks for High-Performance Methane Storage,” *ACS Applied Materials and Interfaces*, vol. 13, no. 20, pp. 23 647–23 654, 5 2021.
- [20] Z. Qiao, K. Zhang, and J. Jiang, “In silico screening of 4764 computation-ready, experimental metal-organic frameworks for CO<sub>2</sub> separation,” *Journal of Materials Chemistry A*, vol. 4, no. 6, pp. 2105–2114, 2016.
- [21] S. M. Cohen, “Postsynthetic methods for the functionalization of metal-organic frameworks,” *Chemical Reviews*, vol. 112, no. 2, pp. 970–1000, 2 2012.
- [22] Z. Cai, C. E. Bien, Q. Liu, and C. R. Wade, “Insights into CO<sub>2</sub> Adsorption in M-OH Functionalized MOFs,” *Chemistry of Materials*, vol. 32, no. 10, pp. 4257–4264, 5 2020.
- [23] S. Chong, G. Thiele, and J. Kim, “Excavating hidden adsorption sites in metal-organic frameworks using rational defect engineering,” *Nature Communications*, vol. 8, no. 1, 12 2017.
- [24] Y. Gu, B. A. Anjali, S. Yoon, Y. Choe, Y. G. Chung, and D. W. Park, “Defect-engineered MOF-801 for cycloaddition of CO<sub>2</sub> with epoxides,” *Journal of Materials Chemistry A*, 2022.
- [25] A. J. White, M. Gibaldi, J. Burner, R. A. Mayo, and T. K. Woo, “High structural error rates in “computation-ready” MOF databases discovered by checking metal oxidation states,” *Journal of the American Chemical Society*, vol. 147, no. 21, pp. 17 579–17 583, 2025, PMID: 40375712. [Online]. Available: <https://doi.org/10.1021/jacs.5c04914>
- [26] X. Jin, S. Garcia, and B. Smit, “Correspondence on "The Open DAC 2023 dataset and challenges for sorbent discovery in direct air capture",” *ACS Central Science*, vol. 11, no. 6, pp. 868–871, May 2025.
- [27] Y.-L. Liao, B. Wood, A. Das, and T. Smidt. EquiformerV2: Improved equivariant transformer for scaling to higher-degree representations. *arXiv (Computer Science, Machine Learning)*, December 2, 2023, ver. 2. [Online]. Available: <https://doi.org/10.48550/arXiv.2306.12059>

- [28] X. Fu, B. M. Wood, L. Barroso-Luque, D. S. Levine, M. Gao, M. Dzamba, and C. L. Zitnick, "Learning smooth and expressive interatomic potentials for physical property prediction," 2025. [Online]. Available: <https://arxiv.org/abs/2502.12147>
- [29] B. M. Wood, M. Dzamba, X. Fu, M. Gao, M. Shuaibi, L. Barroso-Luque, K. Abdelmaqsoud, V. Gharakhanyan, J. R. Kitchin, D. S. Levine, K. Michel, A. Sriram, T. Cohen, A. Das, A. Rizvi, S. J. Sahoo, Z. W. Ulissi, and C. L. Zitnick, "UMA: A family of universal models for atoms," 2025. [Online]. Available: <https://arxiv.org/abs/2506.23971>
- [30] X. Jin, K. M. Jablonka, E. Moubarak, Y. Li, and B. Smit, "Mofchecker: a package for validating and correcting metal-organic framework (MOF) structures," *Digital Discovery*, vol. 4, pp. 1560–1569, 2025. [Online]. Available: <http://dx.doi.org/10.1039/D5DD00109A>
- [31] T. A. Manz and D. S. Sholl, "Chemically meaningful atomic charges that reproduce the electrostatic potential in periodic and nonperiodic materials," *J. Chem. Theory Comput.*, vol. 6, no. 8, pp. 2455–2468, 2010. [Online]. Available: <https://doi.org/10.1021/ct100125x>
- [32] C. E. Wilmer, K. C. Kim, and R. Q. Snurr, "An extended charge equilibration method," *Journal of Physical Chemistry Letters*, vol. 3, no. 17, pp. 2506–2511, 9 2012.
- [33] D. Ongari, P. G. Boyd, O. Kadioglu, A. K. Mace, S. Keskin, and B. Smit, "Evaluating charge equilibration methods to generate electrostatic fields in nanoporous materials," *J. Chem. Theory Comput.*, vol. 15, pp. 382–401, 2019.
- [34] L. M. Brabson, A. J. Medford, and D. S. Sholl, "Comparing classical and machine learning force fields for modeling deformation of solid sorbents relevant for direct air capture," 2025. [Online]. Available: <https://arxiv.org/abs/2506.09256>
- [35] J. Sun, F. Gharagheizi, H. Fang, P. I. Ravikovitch, and D. S. Sholl, "Development of porous crystalline materials for selective binding of O<sub>2</sub> from air," *The Journal of Physical Chemistry C*, vol. 127, no. 1, pp. 776–787, 2023. [Online]. Available: <https://doi.org/10.1021/acs.jpcc.2c07508>
- [36] Z. Zhao, H. Ren, D. Yang, Y. Han, J. Shi, K. An, Y. Chen, Y. Shi, W. Wang, J. Tan, X. Xin, Y. Zhang, and Z. Jiang, "Boosting Nitrogen Activation via Bimetallic Organic Frameworks for Photocatalytic Ammonia Synthesis," *ACS Catalysis*, vol. 11, pp. 9986–9995, 2021.
- [37] F. Zhang, H. Shang, B. Zhai, Z. Zhao, Y. Wang, L. Li, J. Li, and J. Yang, "Synergistic Nitrogen Binding Sites in a Metal-Organic Framework for Efficient N<sub>2</sub>/O<sub>2</sub> Separation," *Angewandte Chemie - International Edition*, vol. 62, no. 50, 12 2023.
- [38] H. Demir, S. J. Stoneburner, W. Jeong, D. Ray, X. Zhang, O. K. Farha, C. J. Cramer, J. I. Siepmann, and L. Gagliardi, "Metal-Organic Frameworks with Metal-Catecholates for O<sub>2</sub>/N<sub>2</sub> Separation," *Journal of Physical Chemistry C*, vol. 123, no. 20, pp. 12 935–12 946, 5 2019.
- [39] R. W. Flaig, T. M. Osborn Popp, A. M. Fracaroli, E. A. Kapustin, M. J. Kalmutzki, R. M. Altamimi, F. Fathieh, J. A. Reimer, and O. M. Yaghi, "The chemistry of CO<sub>2</sub> capture in an amine-functionalized metal-organic framework under dry and humid conditions," *Journal of the American Chemical Society*, vol. 139, no. 35, p. 12125–12128, Sep. 2017. [Online]. Available: <https://pubs.acs.org/doi/10.1021/jacs.7b06382>
- [40] A. M. Fracaroli, H. Furukawa, M. Suzuki, M. Dodd, S. Okajima, F. Gándara, J. A. Reimer, and O. M. Yaghi, "Metal-organic frameworks with precisely designed interior for carbon dioxide capture in the presence of water," *Journal of the American Chemical Society*, vol. 136, no. 25, p. 8863–8866, Jun. 2014. [Online]. Available: <https://pubs.acs.org/doi/10.1021/ja503296c>

- [41] J. Ethiraj, E. Albanese, B. Civalleri, J. G. Vitillo, F. Bonino, S. Chavan, G. C. Shearer, K. P. Lillerud, and S. Bordiga, “Carbon dioxide adsorption in amine-functionalized mixed-ligand metal–organic frameworks of UiO-66 topology,” *ChemSusChem*, vol. 7, no. 12, p. 3382–3388, Dec. 2014. [Online]. Available: <https://chemistry-europe.onlinelibrary.wiley.com/doi/10.1002/cssc.201402694>
- [42] D.-M. Chen, N. Xu, X.-H. Qiu, and P. Cheng, “Functionalization of metal–organic framework via mixed-ligand strategy for selective CO<sub>2</sub> sorption at ambient conditions,” *Crystal Growth & Design*, vol. 15, no. 2, p. 961–965, Feb. 2015. [Online]. Available: <https://pubs.acs.org/doi/10.1021/cg501758a>
- [43] S. S. Dhankhar, N. Sharma, S. Kumar, T. J. D. Kumar, and C. M. Nagaraja, “Rational design of a bifunctional, two-fold interpenetrated ZnII - metal–organic framework for selective adsorption of CO<sub>2</sub> and efficient aqueous phase sensing of 2,4,6-trinitrophenol,” *Chemistry – A European Journal*, vol. 23, no. 64, p. 16204–16212, Nov. 2017. [Online]. Available: <https://chemistry-europe.onlinelibrary.wiley.com/doi/10.1002/chem.201703384>
- [44] Z. H. Rada, H. R. Abid, H. Sun, and S. Wang, “Bifunctionalized metal organic frameworks, UiO-66-NO<sub>2</sub>-N(n = -NH<sub>2</sub>, -(OH)<sub>2</sub>, -(COOH)<sub>2</sub>), for enhanced adsorption and selectivity of CO<sub>2</sub> and N<sub>2</sub>,” *Journal of Chemical & Engineering Data*, vol. 60, no. 7, p. 2152–2161, Jul. 2015. [Online]. Available: <https://pubs.acs.org/doi/10.1021/acs.jced.5b00229>
- [45] Y. Hu, W. M. Verdegaal, S. Yu, and H. Jiang, “Alkylamine-tethered stable metal–organic framework for CO<sub>2</sub> capture from flue gas,” *ChemSusChem*, vol. 7, no. 3, p. 734–737, Mar. 2014. [Online]. Available: <https://chemistry-europe.onlinelibrary.wiley.com/doi/10.1002/cssc.201301163>
- [46] T. K. Vo, W.-S. Kim, and J. Kim, “Ethylenediamine-incorporated MIL-101 (Cr)-NH<sub>2</sub> metal-organic frameworks for enhanced CO<sub>2</sub> adsorption,” *Korean Journal of Chemical Engineering*, vol. 37, no. 7, p. 1206–1211, Jul. 2020. [Online]. Available: <https://link.springer.com/10.1007/s11814-020-0548-8>
- [47] S. Choi, T. Watanabe, T.-H. Bae, D. S. Sholl, and C. W. Jones, “Modification of the Mg/dobdc mof with amines to enhance CO<sub>2</sub> adsorption from ultradilute gases,” *The Journal of Physical Chemistry Letters*, vol. 3, no. 9, p. 1136–1141, May 2012. [Online]. Available: <https://pubs.acs.org/doi/10.1021/jz300328j>
- [48] P.-Q. Liao, X.-W. Chen, S.-Y. Liu, X.-Y. Li, Y.-T. Xu, M. Tang, Z. Rui, H. Ji, J.-P. Zhang, and X.-M. Chen, “Putting an ultrahigh concentration of amine groups into a metal–organic framework for CO<sub>2</sub> capture at low pressures,” *Chemical Science*, vol. 7, no. 10, p. 6528–6533, 2016. [Online]. Available: <https://xlink.rsc.org/?DOI=C6SC00836D>
- [49] M. C. Bernini, A. A. García Blanco, J. Villarroel-Rocha, D. Fairen-Jimenez, K. Sapag, A. J. Ramirez-Pastor, and G. E. Narda, “Tuning the target composition of amine-grafted CPO-27-Mg for capture of CO<sub>2</sub> under post-combustion and air filtering conditions: a combined experimental and computational study,” *Dalton Transactions*, vol. 44, no. 43, p. 18970–18982, 2015. [Online]. Available: <https://xlink.rsc.org/?DOI=C5DT03137K>
- [50] R. L. Siegelman, T. M. McDonald, M. I. Gonzalez, J. D. Martell, P. J. Milner, J. A. Mason, A. H. Berger, A. S. Bhowan, and J. R. Long, “Controlling Cooperative CO<sub>2</sub> Adsorption in Diamine-Appended Mg<sub>2</sub>(dobpdc) Metal-Organic Frameworks,” *Journal of the American Chemical Society*, vol. 139, no. 30, pp. 10 526–10 538, 8 2017.

- [51] T. M. McDonald, J. A. Mason, X. Kong, E. D. Bloch, D. Gygi, A. Dani, V. Crocellà, F. Giordanino, S. O. Odoh, W. S. Drisdell, B. Vlasisavljevich, A. L. Dzubak, R. Poloni, S. K. Schnell, N. Planas, K. Lee, T. Pascal, L. F. Wan, D. Prendergast, J. B. Neaton, B. Smit, J. B. Kortright, L. Gagliardi, S. Bordiga, J. A. Reimer, and J. R. Long, “Cooperative insertion of CO<sub>2</sub> in diamine-appended metal-organic frameworks,” *Nature*, vol. 519, no. 7543, p. 303–308, Mar. 2015. [Online]. Available: <https://www.nature.com/articles/nature14327>
- [52] Z. Yu, S. Jamdade, X. Yu, X. Cai, and D. S. Sholl, “Efficient generation of large collections of metal-organic framework structures containing well-defined point defects,” *The Journal of Physical Chemistry Letters*, vol. 14, no. 29, p. 6658–6665, Jul. 2023. [Online]. Available: <https://pubs.acs.org/doi/10.1021/acs.jpcllett.3c01524>
- [53] B. J. Bucior, A. S. Rosen, M. Haranczyk, Z. Yao, M. E. Ziebel, O. K. Farha, J. T. Hupp, J. I. Siepmann, A. Aspuru-Guzik, and R. Q. Snurr, “Identification schemes for metal-organic frameworks to enable rapid search and cheminformatics analysis,” *Crystal Growth & Design*, vol. 19, no. 11, p. 6682–6697, Nov. 2019. [Online]. Available: <https://pubs.acs.org/doi/10.1021/acs.cgd.9b01050>
- [54] Y. G. Chung, E. Haldoupis, B. J. Bucior, M. Haranczyk, S. Lee, H. Zhang, K. D. Vogiatzis, M. Milisavljevic, S. Ling, J. S. Camp, B. Slater, J. I. Siepmann, D. S. Sholl, and R. Q. Snurr, “Advances, updates, and analytics for the computation-ready, experimental metal-organic framework database: Core mof 2019,” *Journal of Chemical & Engineering Data*, vol. 64, no. 12, p. 5985–5998, Dec. 2019. [Online]. Available: <https://pubs.acs.org/doi/10.1021/acs.jced.9b00835>
- [55] B. Vlasisavljevich, S. O. Odoh, S. K. Schnell, A. L. Dzubak, K. Lee, N. Planas, J. B. Neaton, L. Gagliardi, and B. Smit, “CO<sub>2</sub> induced phase transitions in diamine-appended metal-organic frameworks,” *Chemical Science*, vol. 6, no. 9, p. 5177–5185, 2015. [Online]. Available: <https://xlink.rsc.org/?DOI=C5SC01828E>
- [56] P. J. Milner, R. L. Siegelman, A. C. Forse, M. I. Gonzalez, T. Runčevski, J. D. Martell, J. A. Reimer, and J. R. Long, “A diaminopropane-appended metal-organic framework enabling efficient CO<sub>2</sub> capture from coal flue gas via a mixed adsorption mechanism,” *Journal of the American Chemical Society*, vol. 139, no. 38, p. 13541–13553, Sep. 2017. [Online]. Available: <https://pubs.acs.org/doi/10.1021/jacs.7b07612>
- [57] A. C. Forse, P. J. Milner, J.-H. Lee, H. N. Redfearn, J. Oktawiec, R. L. Siegelman, J. D. Martell, B. Dinakar, L. B. Zasada, M. I. Gonzalez, J. B. Neaton, J. R. Long, and J. A. Reimer, “Elucidating CO<sub>2</sub> chemisorption in diamine-appended metal-organic frameworks,” *Journal of the American Chemical Society*, vol. 140, no. 51, p. 18016–18031, Dec. 2018. [Online]. Available: <https://pubs.acs.org/doi/10.1021/jacs.8b10203>
- [58] Z. Zhu, H. Tsai, S. T. Parker, J.-H. Lee, Y. Yabuuchi, H. Z. H. Jiang, Y. Wang, S. Xiong, A. C. Forse, B. Dinakar, A. Huang, C. Dun, P. J. Milner, A. Smith, P. Guimarães Martins, K. R. Meihaus, J. J. Urban, J. A. Reimer, J. B. Neaton, and J. R. Long, “High-capacity, cooperative CO<sub>2</sub> capture in a diamine-appended metal-organic framework through a combined chemisorptive and physisorptive mechanism,” *Journal of the American Chemical Society*, vol. 146, no. 9, p. 6072–6083, Mar. 2024. [Online]. Available: <https://pubs.acs.org/doi/10.1021/jacs.3c13381>
- [59] E. J. Kim, R. L. Siegelman, H. Z. H. Jiang, A. C. Forse, J.-H. Lee, J. D. Martell, P. J. Milner, J. M. Falkowski, J. B. Neaton, J. A. Reimer, S. C. Weston, and J. R. Long,

- “Cooperative carbon capture and steam regeneration with tetraamine-appended metal–organic frameworks,” *Science*, vol. 369, no. 6502, p. 392–396, Jul. 2020. [Online]. Available: <https://www.science.org/doi/10.1126/science.abb3976>
- [60] K.-Y. Lin, Z.-M. Xie, L.-S. Hong, and J.-C. Jiang, “Insights into the capture mechanism of CO<sub>2</sub> by diamine-appended Mg<sub>2</sub>(dobpdc): a combined dft and microkinetic modeling study,” *Journal of Materials Chemistry C*, vol. 11, no. 38, p. 13085–13094, 2023. [Online]. Available: <https://xlink.rsc.org/?DOI=D3TC01381B>
- [61] W. R. Lee, S. Y. Hwang, D. W. Ryu, K. S. Lim, S. S. Han, D. Moon, J. Choi, and C. S. Hong, “Diamine-functionalized metal–organic framework: exceptionally high CO<sub>2</sub> capacities from ambient air and flue gas, ultrafast CO<sub>2</sub> uptake rate, and adsorption mechanism,” *Energy Environ. Sci.*, vol. 7, no. 2, p. 744–751, 2014. [Online]. Available: <https://xlink.rsc.org/?DOI=C3EE42328J>
- [62] L. A. Darunte, K. S. Walton, D. S. Sholl, and C. W. Jones, “CO<sub>2</sub> capture via adsorption in amine-functionalized sorbents,” *Current Opinion in Chemical Engineering*, vol. 12, p. 82–90, May 2016. [Online]. Available: <https://linkinghub.elsevier.com/retrieve/pii/S2211339816300211>
- [63] S. Lee, B. Kim, H. Cho, H. Lee, S. Y. Lee, E. S. Cho, and J. Kim, “Computational screening of trillions of metal–organic frameworks for high-performance methane storage,” *ACS Applied Materials & Interfaces*, vol. 13, no. 20, pp. 23 647–23 654, 2021, pMID: 33988362. [Online]. Available: <https://doi.org/10.1021/acsami.1c02471>
- [64] T. F. Gonzalez, “Clustering to minimize the maximum intercluster distance,” *Theoretical Computer Science*, vol. 38, pp. 293–306, 1985. [Online]. Available: <https://www.sciencedirect.com/science/article/pii/0304397585902245>
- [65] J. P. Janet and H. J. Kulik, “Resolving transition metal chemical space: Feature selection for machine learning and structure–property relationships,” *The Journal of Physical Chemistry A*, vol. 121, no. 46, pp. 8939–8954, 2017, pMID: 29095620.
- [66] K. M. Jablonka, A. S. Rosen, A. S. Krishnapriyan, and B. Smit, “An ecosystem for digital reticular chemistry,” sep 2022. [Online]. Available: <https://doi.org/10.26434/2Fchemrxiv-2022-4g7rx>
- [67] D. Dubbeldam, S. Calero, D. E. Ellis, and R. Q. Snurr, “RASPA: Molecular simulation software for adsorption and diffusion in flexible nanoporous materials,” *Molecular Simulation*, vol. 42, no. 2, pp. 81–101, 1 2016.
- [68] T. F. Willems, C. H. Rycroft, M. Kazi, J. C. Meza, and M. Haranczyk, “Algorithms and tools for high-throughput geometry-based analysis of crystalline porous materials,” *Microporous and Mesoporous Materials*, vol. 149, no. 1, pp. 134–141, 2 2012.
- [69] K. Schütt, P.-J. Kindermans, H. E. S. Felix, S. Chmiela, A. Tkatchenko, and K.-R. Müller, “SchNet: A continuous-filter convolutional neural network for modeling quantum interactions,” in *Advances in Neural Information Processing Systems*, 2017, pp. 991–1001.
- [70] A. Sriram, A. Das, B. M. Wood, S. Goyal, and C. L. Zitnick, “Towards training billion parameter graph neural networks for atomic simulations,” in *International Conference on Learning Representations*, 2022.
- [71] J. Gastegger, F. Becker, and S. Günnemann, “GemNet: Universal directional graph neural

- networks for molecules,” in *Advances in Neural Information Processing Systems*, vol. 34, 2021, pp. 6790–6802.
- [72] J. Gasteiger, M. Shuaibi, A. Sriram, S. Günnemann, Z. Ulissi, C. L. Zitnick, and A. Das. GemNet-OC: Developing Graph Neural Networks for Large and Diverse Molecular Simulation Datasets. *Transact. Mach. Learn. Res.* **2022**. [Online]. Available: <https://openreview.net/forum?id=u8tvSxm4Bs>
- [73] K. Schütt, O. Unke, and M. Gastegger, “Equivariant message passing for the prediction of tensorial properties and molecular spectra,” in *Proceedings of the 38th International Conference on Machine Learning*. PMLR, 2021, pp. 9377–9388.
- [74] S. Passaro and C. L. Zitnick, “Reducing SO(3) convolutions to SO(2) for efficient equivariant gnns,” in *Proceedings of the 40th International Conference on Machine Learning*, ser. ICML’23, 2023.
- [75] I. Batatia, D. P. Kovacs, G. N. C. Simm, C. Ortner, and G. Csanyi, “MACE: Higher order equivariant message passing neural networks for fast and accurate force fields,” in *Advances in Neural Information Processing Systems*, A. H. Oh, A. Agarwal, D. Belgrave, and K. Cho, Eds., 2022. [Online]. Available: <https://openreview.net/forum?id=YpPngE-ZU>
- [76] K. Abdelmaqsood, M. Shuaibi, A. Kolluru, R. Cheula, and J. R. Kitchin, “Investigating the error imbalance of large-scale machine learning potentials in catalysis,” *Catal. Sci. Technol.*, vol. 14, pp. 5899–5908, 2024.
- [77] R. Tran, J. Lan, M. Shuaibi, B. M. Wood, S. Goyal, A. Das, J. Heras-Domingo, A. Kolluru, A. Rizvi, N. Shoghi, A. Sriram, F. Therrien, J. Abed, O. Voznyy, E. H. Sargent, Z. Ulissi, and C. L. Zitnick, “The Open Catalyst 2022 (OC22) dataset and challenges for oxide electrocatalysts,” *ACS Catalysis*, vol. 13, no. 5, pp. 3066–3084, 2023.
- [78] I. Batatia, P. Benner, Y. Chiang, A. M. Elena, D. P. Kovács, J. Riebesell, X. R. Advincula, M. Asta, M. Avaylon, W. J. Baldwin, F. Berger, N. Bernstein, A. Bhowmik, S. M. Blau, V. Cărare, J. P. Darby, S. De, F. D. Pia, V. L. Deringer, R. Elijošius, Z. El-Machachi, F. Falcioni, E. Fako, A. C. Ferrari, A. Genreith-Schriever, J. George, R. E. A. Goodall, C. P. Grey, P. Grigorev, S. Han, W. Handley, H. H. Heenen, K. Hermansson, C. Holm, J. Jaafar, S. Hofmann, K. S. Jakob, H. Jung, V. Kapil, A. D. Kaplan, N. Karimitari, J. R. Kermode, N. Kroupa, J. Kullgren, M. C. Kuner, D. Kuryla, G. Liepuoniute, J. T. Margraf, I.-B. Magdău, A. Michaelides, J. H. Moore, A. A. Naik, S. P. Niblett, S. W. Norwood, N. O’Neill, C. Ortner, K. A. Persson, K. Reuter, A. S. Rosen, L. L. Schaaf, C. Schran, B. X. Shi, E. Sivonxay, T. K. Stenczel, V. Svahn, C. Sutton, T. D. Swinburne, J. Tilly, C. van der Oord, E. Varga-Umbrich, T. Vegge, M. Vondrák, Y. Wang, W. C. Witt, F. Zills, and G. Csányi, “A foundation model for atomistic materials chemistry,” 2024. [Online]. Available: <https://arxiv.org/abs/2401.00096>
- [79] B. Deng, P. Zhong, K. Jun, J. Riebesell, K. Han, C. J. Bartel, and G. Ceder, “CHGNet as a pretrained universal neural network potential for charge-informed atomistic modelling,” *Nature Machine Intelligence*, vol. 5, no. 9, pp. 1031–1041, 2023.
- [80] Y. Lim, H. Park, A. Walsh, and J. Kim, “Accelerating CO<sub>2</sub> direct air capture screening for metal-organic frameworks with a transferable machine learning force field,” *Matter*, vol. 8, p. 102203, 06 2025.
- [81] D. M. Wood and A. Zunger, “A new method for diagonalising large matrices,” *Journal of Physics A: General Physics*, vol. 18, no. 9, pp. 1343–1359, 1985.

- [82] K. S. Walton and D. S. Sholl, “Predicting multicomponent adsorption: 50 years of the ideal adsorbed solution theory,” *AIChE Journal*, vol. 61, no. 9, pp. 2757–2762, 9 2015.
- [83] D. Frenkel and B. Smit, “Understanding molecular simulation (third edition),” in *Understanding Molecular Simulation*, third edition ed., D. Frenkel and B. Smit, Eds. Academic Press, 2023. [Online]. Available: <https://www.sciencedirect.com/science/article/pii/B9780323902922000064>
- [84] X. Yu, S. Choi, D. Tang, A. J. Medford, and D. S. Sholl, “Efficient models for predicting temperature-dependent henry’s constants and adsorption selectivities for diverse collections of molecules in metal–organic frameworks,” *J. Phys. Chem. C*, vol. 125, no. 32, pp. 18 046–18 057, 2021. [Online]. Available: <https://doi.org/10.1021/acs.jpcc.1c05266>
- [85] A. K. Rappe, C. J. Casewit, K. S. Colwell, W. A. I. Goddard, and W. M. Skiff, “Uff, a full periodic table force field for molecular mechanics and molecular dynamics simulations,” *Journal of the American Chemical Society*, vol. 114, no. 25, pp. 10 024–10 035, 1992. [Online]. Available: <https://doi.org/10.1021/ja00051a040>
- [86] G. Pizzi, A. Cepellotti, R. Sabatini, N. Marzari, and B. Kozinsky, “Aiiida: automated interactive infrastructure and database for computational science,” *Computational Materials Science*, vol. 111, pp. 218–230, 2016. [Online]. Available: <https://www.sciencedirect.com/science/article/pii/S0927025615005820>
- [87] J. J. Potoff and J. I. Siepmann, “Vapor–liquid equilibria of mixtures containing alkanes, carbon dioxide, and nitrogen,” *AIChE Journal*, vol. 47, no. 7, pp. 1676–1682, 2001. [Online]. Available: <https://aiche.onlinelibrary.wiley.com/doi/abs/10.1002/aic.690470719>
- [88] A. H. Larsen, J. J. Mortensen, J. Blomqvist, I. E. Castelli, R. Christensen, M. Duřak, J. Friis, M. N. Groves, B. Hammer, C. Hargus, E. D. Hermes, P. C. Jennings, P. B. Jensen, J. Kermode, J. R. Kitchin, E. L. Kolsbjerg, J. Kubal, K. Kaasbjerg, S. Lysgaard, J. B. Maronsson, T. Maxson, T. Olsen, L. Pastewka, A. Peterson, C. Rostgaard, J. Schiřtz, O. Schütt, M. Strange, K. S. Thygesen, T. Vegge, L. Vilhelmsen, M. Walter, Z. Zeng, and K. W. Jacobsen, “The atomic simulation environment—a python library for working with atoms,” *Journal of Physics: Condensed Matter*, vol. 29, no. 27, p. 273002, 2017. [Online]. Available: <http://stacks.iop.org/0953-8984/29/i=27/a=273002>
- [89] C. Charalambous, E. Moubarak, J. Schilling, E. Sanchez Fernandez, J.-Y. Wang, L. Her-raiz, F. McIlwaine, S. Peh, M. Garvin, K. Jablonka, S. Moosavi, J. Herck, A. Yurdusen, A. Pourghaderi, A.-Y. Song, G. Mouchaham, C. Serre, J. Reimer, A. Bardow, and S. García, “A holistic platform for accelerating sorbent-based carbon capture,” *Nature*, vol. 632, pp. 89–94, 07 2024.
- [90] J. Park, J. D. Howe, and D. S. Sholl, “How Reproducible Are Isotherm Measurements in Metal-Organic Frameworks?” *Chemistry of Materials*, vol. 29, no. 24, pp. 10 487–10 495, 12 2017.
- [91] Z. Yu, D. M. Anstine, S. E. Boulfefel, C. Gu, C. M. Colina, and D. S. Sholl, “Incorporating flexibility effects into metal–organic framework adsorption simulations using different models,” *ACS Appl. Mater. Interfaces*, vol. 13, no. 51, pp. 61 305–61 315, 2021.
- [92] G. Kresse and J. Hafner, “Ab initio molecular dynamics for liquid metals,” *Physical Review B*, vol. 47, no. 1, p. 558, 1993.

- [93] G. Kresse and J. Furthmüller, “Efficient iterative schemes for ab initio total-energy calculations using a plane-wave basis set,” *Physical Review B*, vol. 54, no. 16, p. 11169, 1996.
- [94] G. Kresse and D. Joubert, “From ultrasoft pseudopotentials to the projector augmented-wave method,” *Physical Review B*, vol. 59, no. 3, p. 1758, 1999.
- [95] R.-B. Lin, D. Chen, Y.-Y. Lin, J.-P. Zhang, and X.-M. Chen, “A zeolite-like zinc triazolate framework with high gas adsorption and separation performance,” *Inorganic Chemistry*, vol. 51, no. 18, p. 9950–9955, Sep. 2012. [Online]. Available: <https://pubs.acs.org/doi/10.1021/ic301463z>
- [96] X.-Y. Chen, B. Zhao, W. Shi, J. Xia, P. Cheng, D.-Z. Liao, S.-P. Yan, and Z.-H. Jiang, “Microporous metal–organic frameworks built on a Ln<sub>3</sub> cluster as a six-connecting node,” *Chemistry of Materials*, vol. 17, no. 11, p. 2866–2874, May 2005. [Online]. Available: <https://pubs.acs.org/doi/10.1021/cm050526o>
- [97] X. Chen, X. Feng, Z. Zhang, X. Deng, F. Dai, L. Zhang, and S. W. Ng, “Multifunctional lanthanide metal–organic frameworks based on -NH<sub>2</sub> modified ligand: Fluorescent ratio probe, CrO<sub>4</sub><sup>2-</sup> ions adsorption, and photocatalytic property,” *Inorganic Chemistry*, vol. 62, no. 39, p. 16170–16181, Oct. 2023.
- [98] R. K. Deshpande, J. L. Minnaar, and S. G. Telfer, “Thermolabile groups in metal–organic frameworks: Suppression of network interpenetration, post-synthetic cavity expansion, and protection of reactive functional groups,” *Angewandte Chemie International Edition*, vol. 49, no. 27, p. 4598–4602, Jun. 2010. [Online]. Available: <https://onlinelibrary.wiley.com/doi/10.1002/anie.200905960>
- [99] S. A. Diamantis, A. D. Pournara, A. G. Hatzidimitriou, M. J. Manos, G. S. Papaefstathiou, and T. Lazarides, “Two new alkaline earth metal organic frameworks with the diamino derivative of biphenyl-4,4'-dicarboxylate as bridging ligand: Structures, fluorescence and quenching by gas phase aldehydes,” *Polyhedron*, vol. 153, p. 173–180, Oct. 2018. [Online]. Available: <https://linkinghub.elsevier.com/retrieve/pii/S0277538718303978>
- [100] W. Fan, H. Lin, X. Yuan, F. Dai, Z. Xiao, L. Zhang, L. Luo, and R. Wang, “Expanded porous metal–organic frameworks by scsc: Organic building units modifying and enhanced gas-adsorption properties,” *Inorganic Chemistry*, vol. 55, no. 13, p. 6420–6425, Jul. 2016. [Online]. Available: <https://pubs.acs.org/doi/10.1021/acs.inorgchem.6b00278>

# Appendix

## A Density Functional Theory Settings

All DFT calculations used VASP version 6.3 [92–94] with the PBE exchange-correlation functional and D3 van der Waals correction (IVDW = 12). VASP 5.4 PBE pseudopotentials were employed with a plane-wave energy cutoff of 600 eV and electronic convergence of 1e-5 eV. Structural relaxations used the conjugate gradient algorithm with forces converged to 0.05 eV/Å or a maximum of 2000 ionic steps. Bare MOFs were relaxations allowed relaxation of lattice parameters (ISIF = 3), while MOF+adsorbate systems used fixed lattice parameters (ISIF = 2) to maintain consistent unit cells for binding energy calculations. Gaussian smearing ( $\sigma = 0.2$  eV) was applied with symmetry disabled to allow proper adsorbate-framework relaxation. See Listing 1 for the full INCAR file

```
ENCUT = 600.000000
POTIM = 0.010000
SIGMA = 0.200000
EDIFF = 1.00e-05
EDIFFG = -5.00e-02
ALGO = NORMAL
GGA = PE
PREC = Accurate
IBRION = 2
ISIF = 2
ISMEAR = 0
ISPIN = 2
ISTART = 0
ISYM = 0
MAXMIX = 40
NELM = 120
NELMIN = 2
NSW = 2000
NWRITE = 2
IVDW = 12
NCORE = 4
LCHARG = .FALSE.
LDIAG = .TRUE.
LPLANE = .TRUE.
LWAVE = .FALSE.
LREAL = Auto
```

**Listing 1** Example INCAR file showing the VASP settings used in creating the ODAC25 dataset. ISIF is set to 2 for MOF + adsorbate calculations (only atomic positions are optimized), and to 3 for bare MOF relaxations (both atom positions and lattice parameters are optimized).

## B K-point Corrections

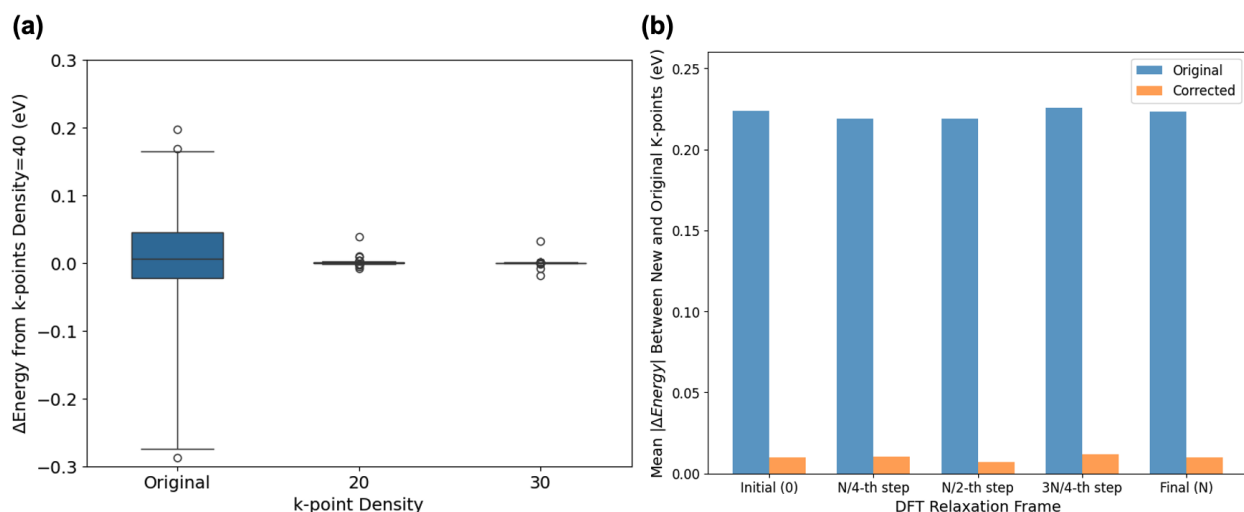


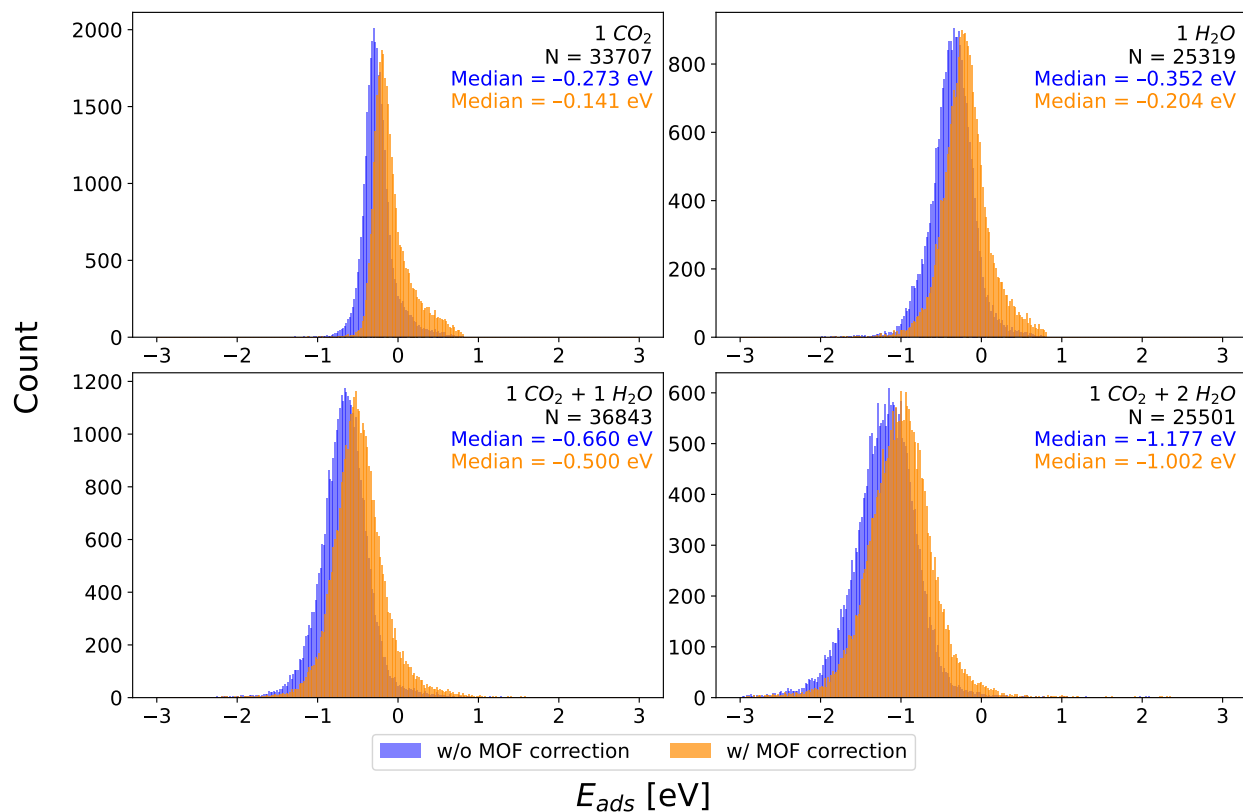
**Figure S1** Approximating higher k-point calculations. (a) Distribution of energy differences from reference calculations with k-point density  $K = 40 \text{ \AA}$ . (b) Mean absolute energy errors across relaxation frames before and after energy correction. The mean error reduces significantly after correction to  $\sim 0.01 \text{ eV}$ .

## C MOFChecker Analysis

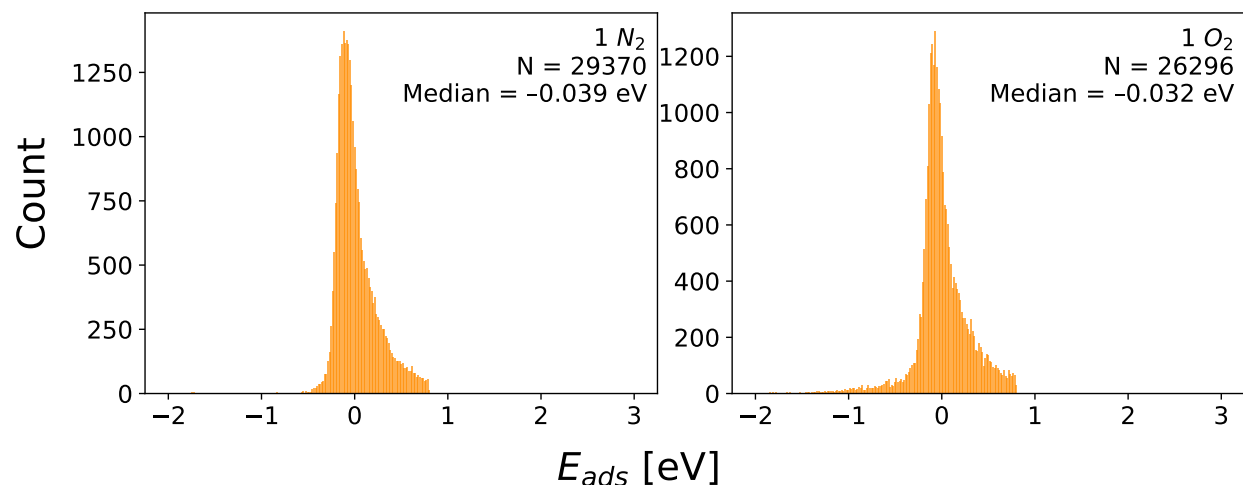
**Table S1** Error rates from MOFChecker v0.9.6 checks split by MOF types

Check	ODAC23 pristine [%]	ODAC23 defective [%]	ODAC25 functionalized [%]	All MOFs [%]
has_metal	0.02	0	0	< 0.01
has_carbon	4.4	6.6	0	4.1
has_hydrogen	10.4	0	0	3.5
has_atomic_overlaps	0	0	0	0
has_overcoordinated_carbon	0.5	0.03	0	0.2
has_overcoordinated_nitrogen	0	0	0	0
has_overcoordinated_hydrogen	0	0	0	0
has_undercoordinated_carbon	10.9	23.6	13.3	16.7
has_undercoordinated_nitrogen	5.9	11.0	0.7	6.6
has_undercoordinated_rare_earth	0.02	0.06	0	0.03
has_undercoordinated_alkali(ne)	0.5	0.7	0	0.4
has_lone_molecule	10.3	32.2	23.4	22.6
has_high_charges	1.0	0.8	0	0.7
has_suspicious_terminal_oxo	0.2	1.4	1.4	1.0
has_geometrically_exposed_metal	6.5	8.5	2.9	6.4

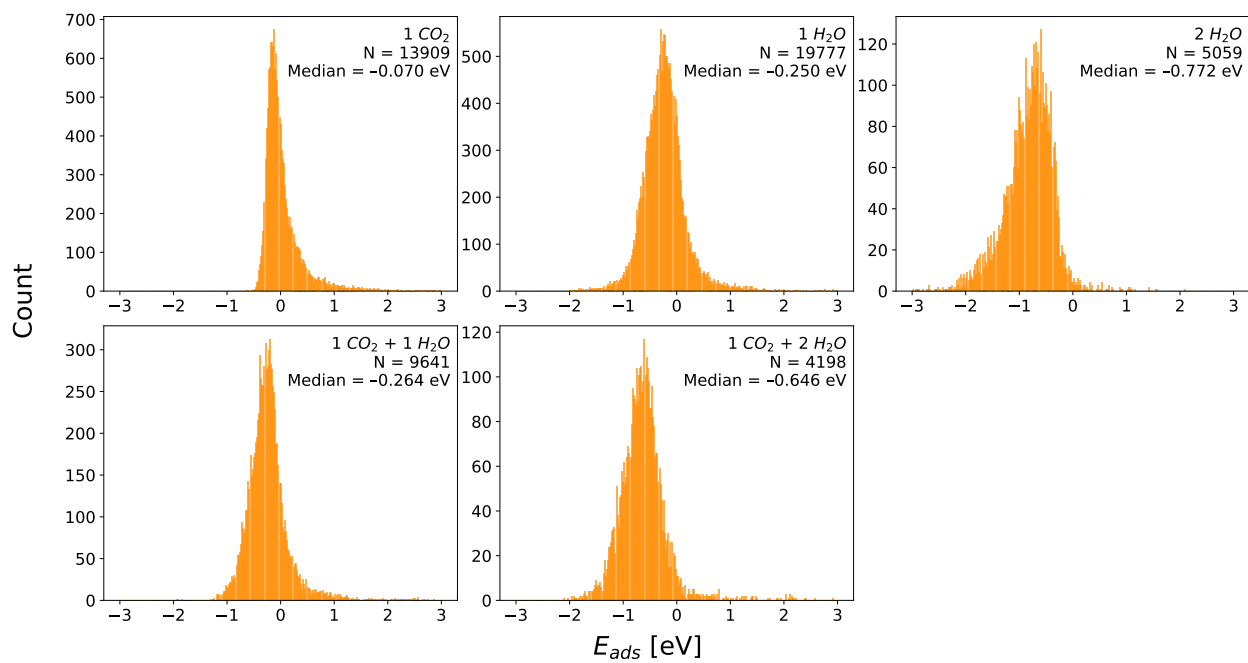
## D Adsorption Energy Distributions



**Figure S2** Distribution of  $\text{CO}_2$  and  $\text{H}_2\text{O}$  adsorption energies in pristine and defective ODAC23 MOFs featuring empty MOF re-relaxations and split by adsorbate type(s). Blue histograms are for adsorption energies presented in ODAC23 without MOF re-relaxations; orange histograms are adsorption energies using the global empty MOF reference energy from all ODAC25 configurations with a given MOF.

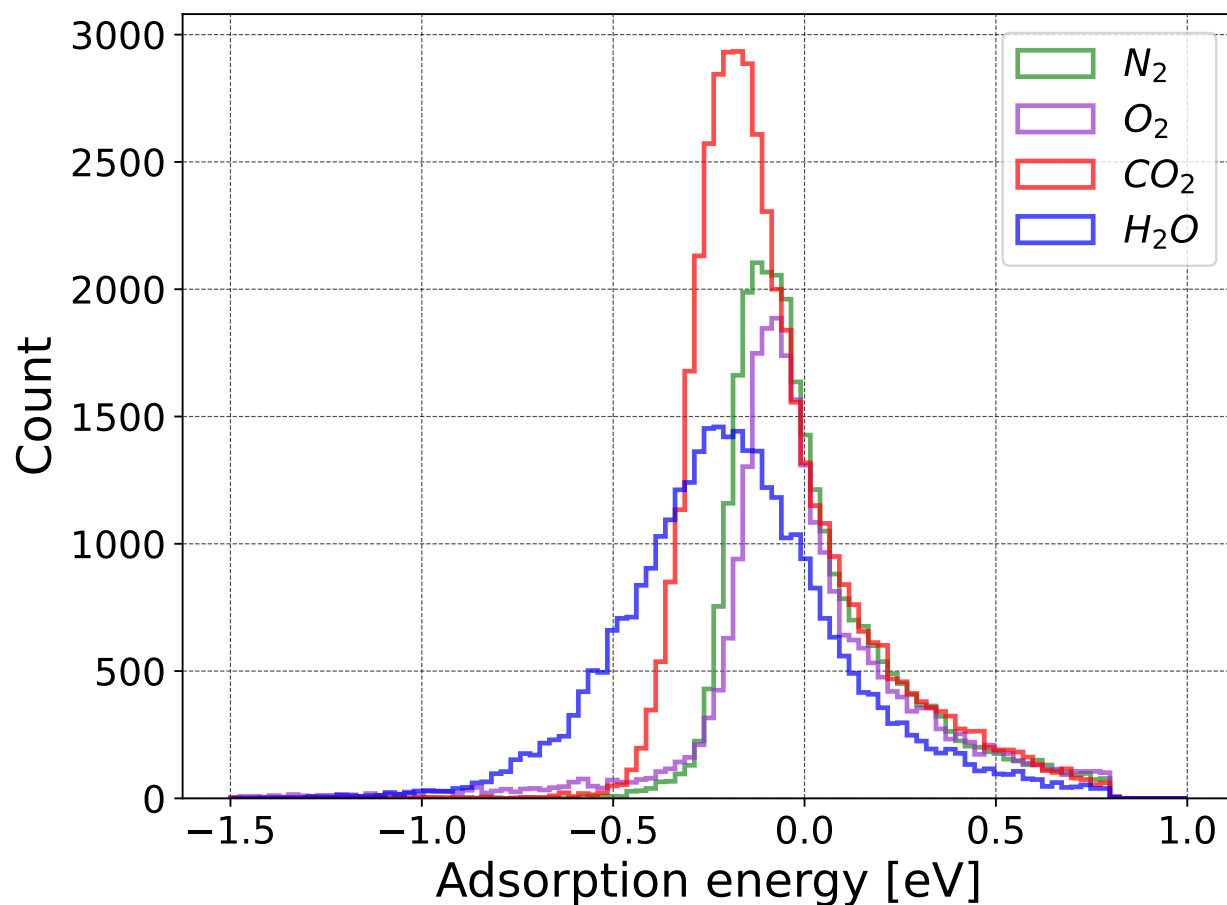


**Figure S3** Distribution of  $\text{N}_2$  and  $\text{O}_2$  adsorption energies in pristine and defective MOFs split by adsorbate type.

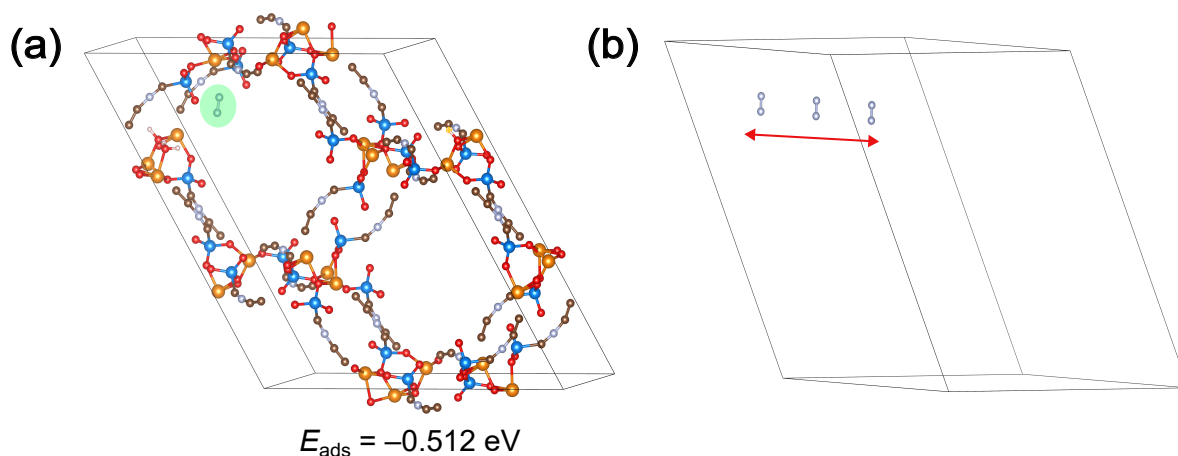


**Figure S4** Distribution of adsorption energies in functionalized MOFs split by adsorbate type(s).

## E $N_2$ Adsorption

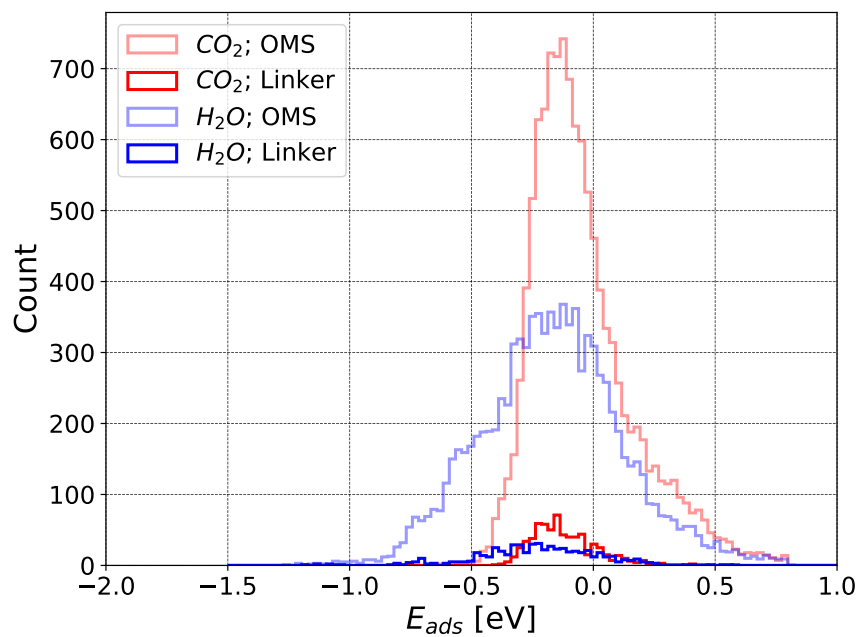


**Figure S5** Histogram of  $CO_2$ ,  $H_2O$ ,  $N_2$ , and  $O_2$  adsorption energies in ODAC23 MOFs split by adsorbate.

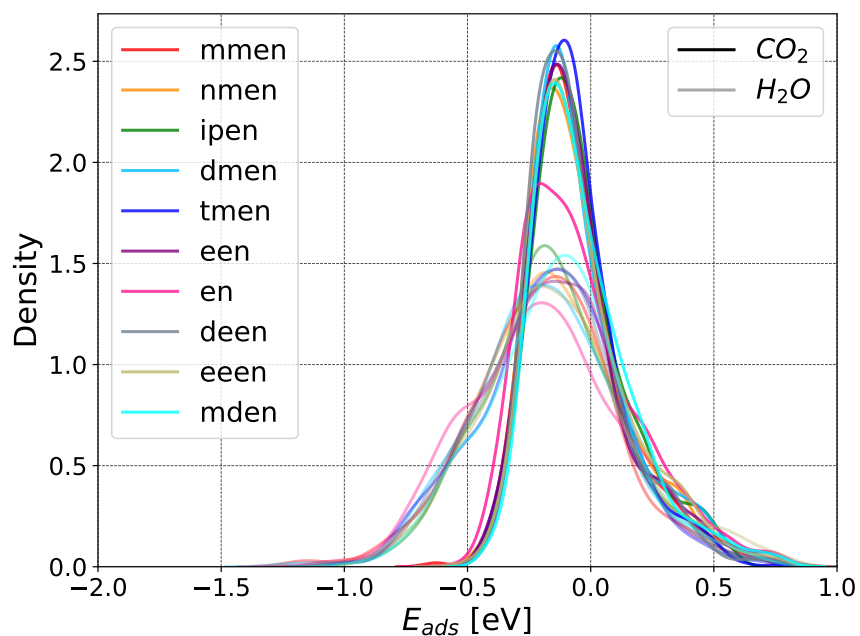


**Figure S6**  $N_2$  physisorption in defective MOF with CSD code QOVDEL. (a) DFT-relaxed MOF+N<sub>2</sub> configuration. (b)  $1 \times 1 \times 3$  supercell in the specified direction with MOF atoms deleted. The narrow unit cell and close proximity of  $N_2$  molecules leads to strong adsorbate-adsorbate interactions. Zn, C, O, H, and N atoms are shown in blue, brown, red, white, and silver, respectively.

## F MOF Functionalization

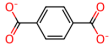
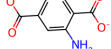
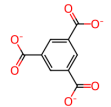
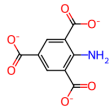
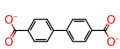
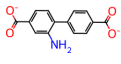
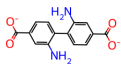
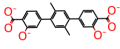
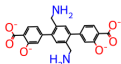
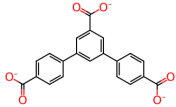
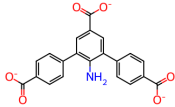


**Figure S7** Histogram of CO<sub>2</sub> and H<sub>2</sub>O adsorption energies in functionalized MOFs split by adsorbate and functionalization type.

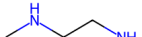
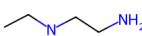
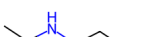
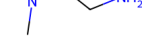
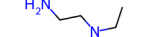
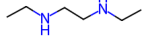


**Figure S8** Kernel density estimation for CO<sub>2</sub> and H<sub>2</sub>O adsorption energies in functionalized MOFs split by diamine used for functionalization.

**Table S2** Linkers used to generate functionalized MOFs via linker functionalization.

Linker Structure	Functionalized Linker Structure	Reference
		[95]
		[96]
		[97]
		[98]
		[99]
		[39]
		[100]

**Table S3** Diamine structures used for open metal site functionalization, spanning primary (1°), secondary (2°), and tertiary (3°) amine classifications with their chemical structures and abbreviations.

Diamine Name	Diamine Structure	Abbreviation	Classification
Ethylenediamine		en	1°/1°
N-Methylethylenediamine		nmen	1°/2°
N-Ethylethylenediamine		een	1°/2°
N-Isopropylethylenediamine		ipen	1°/2°
N,N-Dimethylethylenediamine		dmen	1°/3°
N,N-Diethylethylenediamine		deen	1°/3°
Dimethylethylenediamine		mmen	2°/2°
N,N'-Diethylethylenediamine		eeen	2°/2°
N,N,N'-Trimethylethylenediamine		mden	2°/3°
N,N,N',N'-Tetramethylethylenediamine		tmen	3°/3°

1°: Primary, 2°: Secondary, 3°: Tertiary

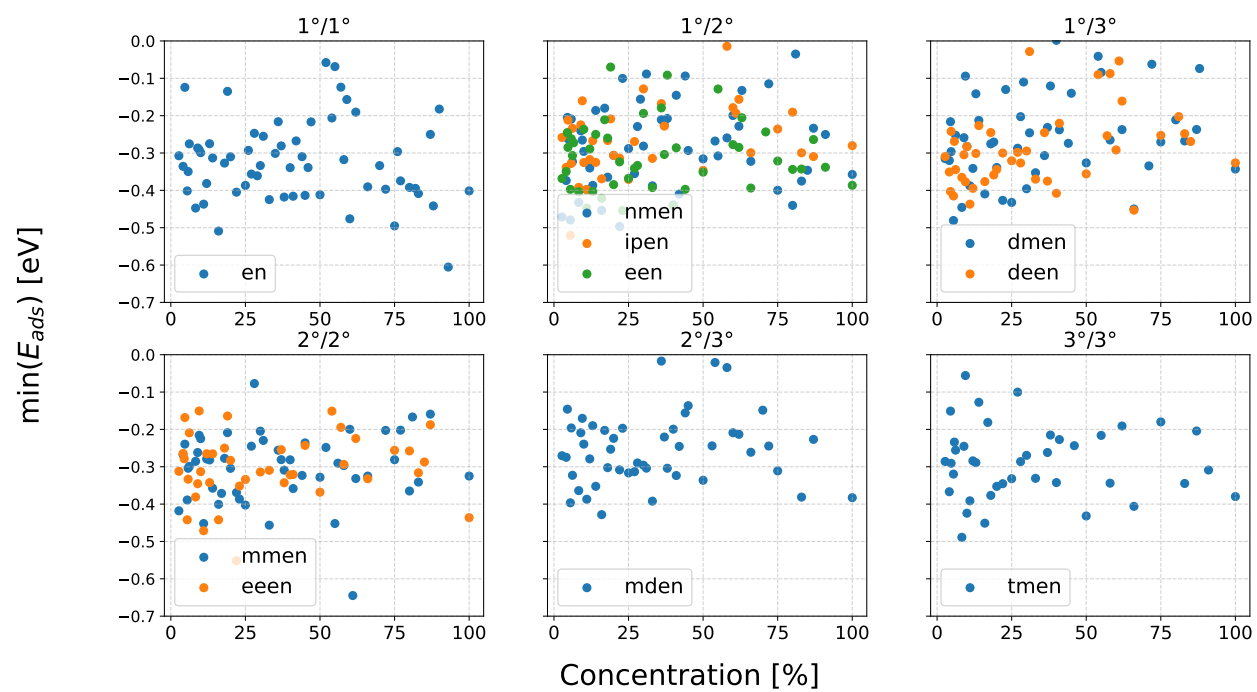


**Figure S9** Minimum CO<sub>2</sub> adsorption energies in MOFs functionalized with the specified diamine as a function of diamine concentration. Diamine codes correspond to [table S3](#).

## G GCMC Placements

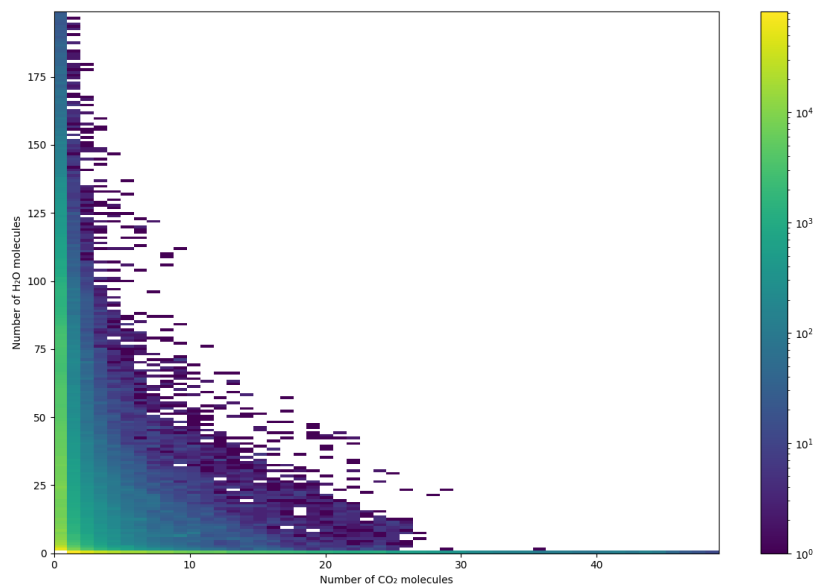


**Figure S10** Two-dimensional histogram showing the distribution of CO<sub>2</sub> and H<sub>2</sub>O molecule counts in GCMC-generated configurations.

## H Synthetic MOF Properties

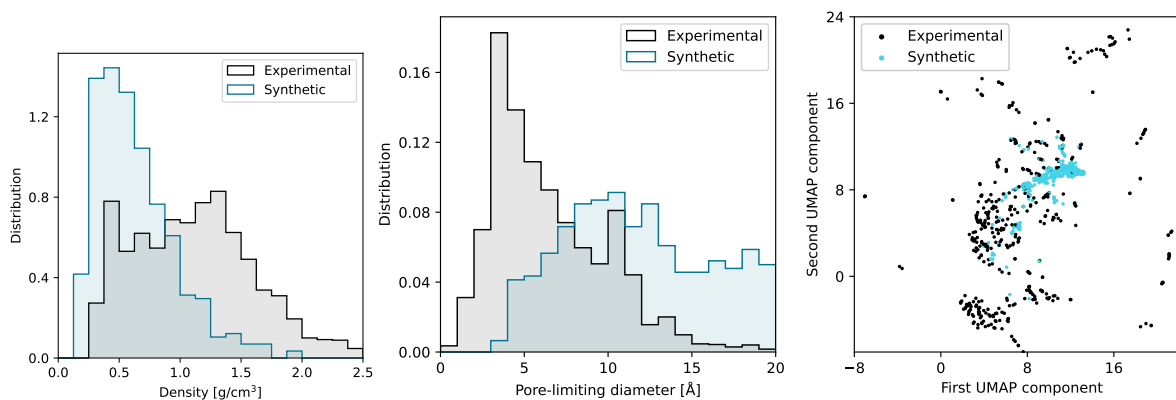


**Figure S11** Properties of synthetically generated MOFs (blue) compared to experimental structures (black). Left: density distribution. Middle: distribution of the PLD. Right: two-dimensional UMAP projection, where for legibility we only show 500 experimental MOFs uniformly sampled from the dataset.

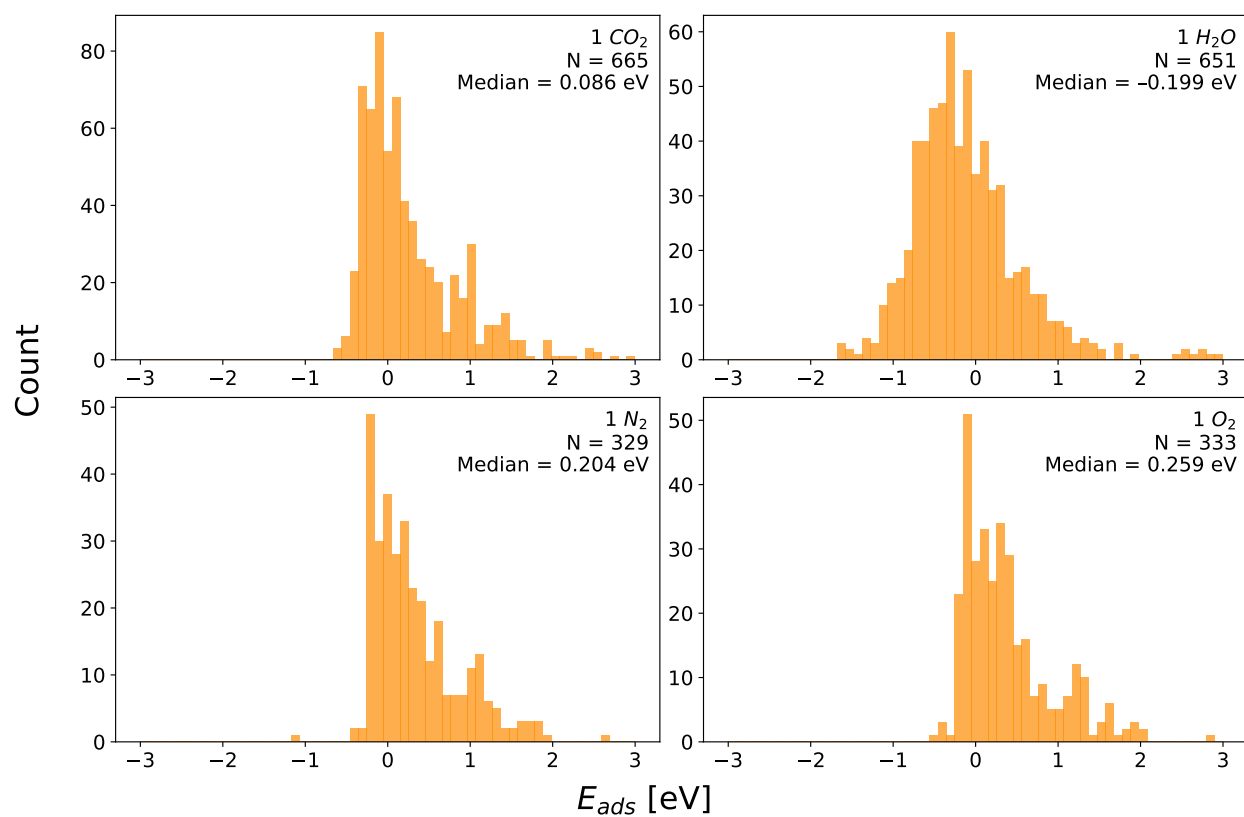


**Figure S12** Distribution of single-molecule adsorption energies in synthetic MOFs split by adsorbate type.

## I Widom Insertion

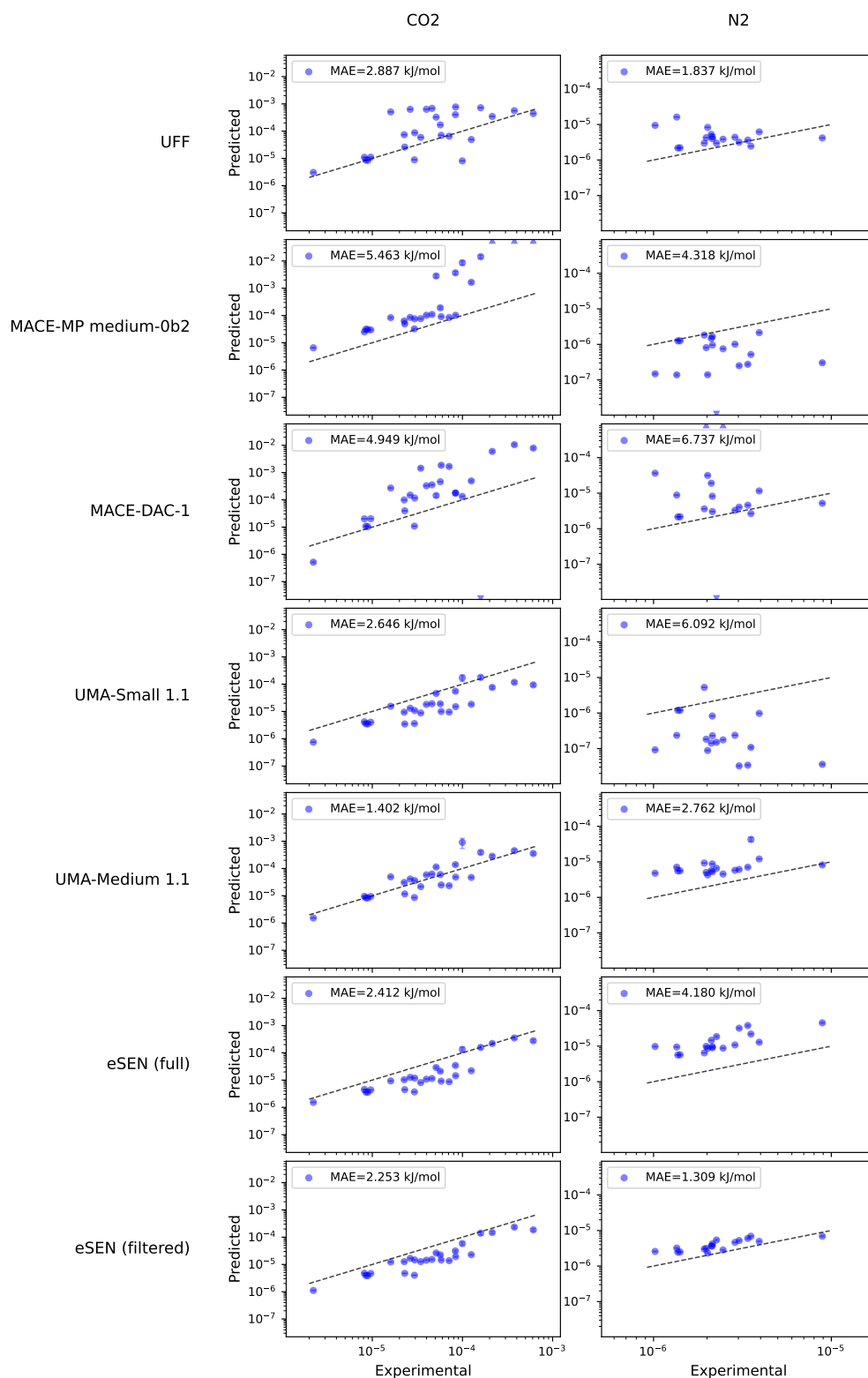


**Figure S13** Log-log scatterplot of the Henry coefficient from experiment and from Widom insertion for the UFF baseline and different MLFFs, with the adsorbates CO<sub>2</sub> and N<sub>2</sub>. We show the mean absolute error of the logarithm of the Henry coefficient in kJ/mol [84], and the standard deviation of the predicted coefficient.

## J MLIP Hyperparameters

Table S4 summarizes the hyperparameters of the eSEN [28] models trained on ODAC25 dataset, as described in section 3.1. The eSEN models were trained in two stages: first, a direct model with a maximum of 30 neighbors, and, subsequently, an energy-conserving model with up to 300 neighbors was trained. We limit the fine-tuning stage to structures with less than 350 atoms to reduce the GPU memory usage. Detailed descriptions of the eSEN model and architecture details are described in Fu et al.[28].

**Table S4** Hyperparameters and training details for the eSEN [28] model trained on the ODAC25 dataset. Comma-separated values indicate pre-training, post-training parameters.

Hyperparameters	eSEN-ODAC25
Number of parameters	50M
Maximum number of neighbors	30, 300
Cutoff radius (Å)	6
Number of layers	10
Number of sphere channels	128
Number of edge channels	128
Maximum degree $L_{max}$	4
Maximum order $M_{max}$	2
Distance function	gaussian
Number of distance basis	128
Number of hidden channels	128
Normalization type	rms_norm_sh
Activation type	gate
ff_type	spectral
Number of GPUs	64
Optimizer	AdamW
Learning rate scheduling	Cosine
Warmup epochs	0.01
Warmup factor	0.2
Maximum learning rate	$8 \times 10^{-4}$
Minimum learning rate factor	0.01
Gradient clipping norm threshold	100
Weight decay	$1 \times 10^{-3}$
Batch size	2000 atoms
Number of epochs	4, 2
Energy loss coefficient	1, 20
Force loss coefficient	20, 16